energies

MDPI

Article

Steady-State and Transient Operation of Solid Oxide Fuel Cell Systems with Anode Off-Gas Recirculation within a Highly Constrained Operating Range

Jan Hollmann * and Stephan Kabelac

Institute of Thermodynamics, Leibniz University Hannover, 30167 Hannover, Germany; kabelac@ift.uni-hannover.de
* Correspondence: hollmann@ift.uni-hannover.de; Tel.: +49-511-762-4601

Abstract: Based on a prototype presented in a prior publication, this research investigates the operational characteristics of a methane-fueled solid oxide fuel cell (SOFC) system with anode off-gas recirculation (AOGR) for electrical energy supply on sea-going vessels. The proposed first-principle system model utilizes a spatially segmented SOFC stack and lumped balance of plant components validated on the component level to accurately depict the steady-state and transient operating behavior. Five operational limitations are chosen to highlight permissible operating conditions with regard to stack and pre-reformer degradation. Steady-state operating maps are presented, emphasizing efficient operating conditions at maximum stack fuel utilization and minimal permissible oxygen-to-carbon ratio. Exemplary transient load changes illustrate increasing system control complexity caused by gas flow delays due to the spatially distributed plant layout. Actuation strategies are presented and underline the need for a top-level model predictive system controller to assure a dynamic and efficient operation within the defined constraints.

Keywords: solid oxide fuel cells; anode off-gas recirculation; dynamic system modeling; system control

Citation: Hollmann, J.; Kabelac, S. Steady-State and Transient Operation of Solid Oxide Fuel Cell Systems with Anode Off-Gas Recirculation within a Highly Constrained Operating Range. *Energies* **2023**, *16*, 7827. https://doi.org/10.3390/en16237827

Academic Editor: Orazio Barbera

Received: 13 September 2023
Revised: 2 November 2023
Accepted: 22 November 2023
Published: 28 November 2023

1. Introduction

The maritime industry is facing a growing demand for greenhouse gas emission reduction as it accounts for almost 3% of global anthropogenic CO_2 emissions [1]. Substituting the current industry standard, heavy fuel oil, with alternative fuels from either biomass or synthetic origins, is considered a major lever. Possible options include hydrogen, methane, methanol, and ammonia, each featuring characteristic advantages and disadvantages in terms of energy density, bunkering availability, expected costs, and safety concerns [2]. However, the future of marine fuels for sea-going vessels remains uncertain, as no clear industry standard is expected by 2050 [3]. Solid oxide fuel cell (SOFC) systems present a promising alternative for electrical energy supply on sea-going vessels due to their fuel flexibility, covering all of the above-mentioned energy carriers [4] at high conversion efficiencies exceeding 60% LHV, as experimentally demonstrated for methane [5]. The deployment of SOFC systems on ships is currently the subject of several research projects, using natural gas [6,7], diesel [8,9], or ammonia as a fuel [10]. Apart from establishing higher power densities and system lifetimes, dynamic and robust system operation is the subject of both the current research and this publication.

State-of-the-art hydrocarbon-fueled SOFC systems typically utilize the concept of anode-off gas recirculation (AOGR), as the steam necessary for fuel reforming is internally provided by the anode off-gas. A principle sketch of AOGR is depicted in Figure 1. Recirculation is typically achieved by high-temperature blowers or ejectors that feedback a certain share of the anode exhaust, defined as the recirculation ratio:

$$RR = \frac{\dot{n}_{\mathrm{AOG,rec}}}{\dot{n}_{\mathrm{AOG,tot}}} \cdot 100\%. \quad (1)$$

This yields the potential of increasing the overall electrochemical fuel utilization FU_{sys}:

$$FU_{\mathrm{sys}} = \frac{FU_{\mathrm{stack}}}{1 - RR(1 - FU_{\mathrm{stack}})}, \tag{2}$$

resulting in higher electrical system net efficiencies without increasing the constrained utilization on stack level $FU_{\mathrm{stack,max}} \approx 75 \ldots 80\%$ to avoid fuel starvation and Ni oxidation at the anode. However, efficiency increase is partly compensated as not only excess hydrogen and steam, but also the reforming products, CO and CO_2, are recirculated, which decreases the hydrogen partial pressure at the anode inlet and, thus, the cell voltage [11].

In addition to the upper limit on FU_{stack}, the composition of the pre-reforming anode gas represents a further operating limit, which is given by the oxygen-to-carbon ratio (O/C). If pure methane as fuel is assumed, O/C can be formulated using the expressions above and a stationary mass balance of the depicted recirculation, yielding:

$$O/C := \frac{\dot{n}_{\mathrm{O}}}{\dot{n}_{\mathrm{C}}} = 4 \cdot RR \cdot FU_{\mathrm{sys}}. \tag{3}$$

The lower limit of this parameter depends on the pre-reforming reaction temperature $O/C_{\mathrm{min}} = f(T)$, as carbon deposition on the catalytic surfaces may occur otherwise. As shown in previous studies, operation in the boundary region ($FU_{\mathrm{stack}} \approx FU_{\mathrm{stack,max}}; O/C \approx O/C_{\mathrm{min}}$) is desirable with regard to high system efficiencies [12,13].

With regard to the dynamics of such a system, two relevant effects in different time domains have to be considered [14]: (i) The dynamics of the gas residence times in the component and pipe volumes. These phenomena occur in the range of several seconds and are coupled by the recirculation loop with the corresponding time delay of the mass flow; (ii) the dynamics due to the thermal inertia of all solids interacting with the gas flows. These corresponding time constants, depending on the ratio of volume flow to component mass, are significantly higher in the range of several minutes.

In terms of system operation and control, AOGR, therefore, leads to a higher degree of complexity, as the system can be considered a coupled and constrained nonlinear multi-variable control problem. Three manipulated variables (MVs), depicted as red arrows in Figure 1, namely the molar fuel flow $\dot{n}_{\mathrm{fuel}}$, the electrical stack current I, as well as the electrical rotation frequency of the recirculation blower $f_{\mathrm{bl,rec}}$, proportional to the rotational shaft speed, affect the behavior of the anodic gas supply. Several aspects not depicted in Figure 1 may further increase the nonlinear plant behavior and control complexity: (i) AOGR typically features a set of heat exchangers in order to preheat the anode inlet gas and to utilize the released heat of the depleted combustibles in an afterburner, thus adding nonlinear thermal coupling in the recirculation loop. (ii) Higher levels of system heat integration can be achieved if the cathode off-gas is not only utilized for heat recuperation but also to oxidize the depleted AOG in the afterburner. This leads to a coupling of cathode molar flow and pre-reforming temperature, thus adding a fourth manipulated variable to the recirculation loop behavior.

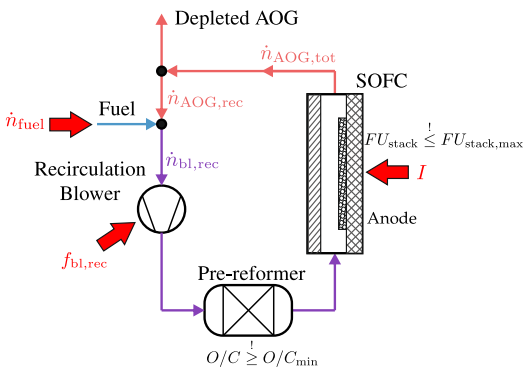

Figure 1. Principle schematics of anode off-gas recirculation.

In contrast to systems in stationary land-based applications, the use of these systems as a central component of the electrical power supply on sea-going ships places significantly higher demands on the dynamic mode of operation and robustness. The systems must deliver a high load change capability in order to be economically used in conjunction with battery storage systems [15], while continuously remaining within the above-mentioned permissible operating window and operating as efficiently and reliably as possible.

In order to meet these criteria, a top-level control is required to supervise the stack as well as the anode and cathode gas supply together to enable power load-following trajectories e.g., given by the ship energy management system. Several multi-variable control strategies, such as conventional PID control, model predictive control (MPC), and fuzzy logic control, have been investigated in the recent past [16], both on the SOFC stack and system level. MPC concepts are of particular interest, as highly nonlinear plant characteristics can be considered and constraints of state variables that are not directly measurable can be directly implemented in the control scheme. This is achieved by state estimation combined with an internal dynamic plant prediction model to minimize a cost function for calculating the next set of MV values in real time. The accuracy of MPC highly depends on the quality of the implemented plant model.

Within this context, the publication aims to deliver:

- **An appropriate first principle modeling approach** of a recently developed SOFC system, which will be explained in Section 2. The model is defined in state-space representation in order to (i) act as a reliable and accurate plant model to predict the operation boundaries in this publication and (ii) form the basis for a reduced plant model to be used in an MPC in a follow-up publication. The model is based on state-of-the-art literature approaches and is presented in Section 3.
- **A comprehensive overview of the permissible steady-state operating range** presented in Section 4 and constrained by a set of operating limits associated with stack degradation. Appropriate system operating parameters will be presented as a function of both electrical load and stack degradation. Evaluation will be based on the system's net efficiency and thermal gradients inside the stack.
- **An assessment of the characteristic transient plant behavior** considering the gas flow dynamics in a spatially separated AOGR setup. This will be based on exemplary load changes presented in Section 5 from which transient operating limitations will be highlighted.

The study closes with generalized recommendations for model-based control strategies of the investigated system layout. The results obtained form the basis of MPC implementation, parameterization, and control accuracy evaluation in a subsequent publication.

2. Plant Layout

In this study, a methane-fueled SOFC system with AOGR is examined, which was developed within the *MultiSchIBZ* research project and already explained in detail in a prior publication [7] (see Figure 2). The design objective was focused on a parallel setup of one or multiple fuel cell modules (FCMs) and a central fuel processing module (FPM). Spatial separation of the pre-reformer and the SOFCs is not advantageous from the perspective of heat integration but offers the advantage of a modular design and comparatively easy replaceability of degraded stack modules and materials like catalysts. The use of different fuels is achieved by only adjusting the FPM in its layout whereas the fuel cell modules may remain unchanged.

The non-recirculated off-gas is catalytically combusted in an oxidation unit. The resulting exhaust gas is utilized to provide heat to the allothermal pre-reformer. A two-stage pre-reforming setup with an adiabatic stage upstream was chosen in order to achieve the highest possible heat transfer to the recirculation loop. Additional heat exchangers are utilized for heat recuperation as the recirculation blower may only be operated up to a limiting temperature. In case internal AOG recuperation is not sufficient, an additional AOG cooler withdraws the remaining heat to reach the desired blower inlet temperature. In contrast to concepts reported in the literature [6,12,17,18], the cathode air supply of the FCMs and the air supply of the oxidation unit are separated due to the modular concept.

This is a slight drawback for the system's net efficiency as an additional air blower is required compared to integrated concepts but allows for independent temperature control.

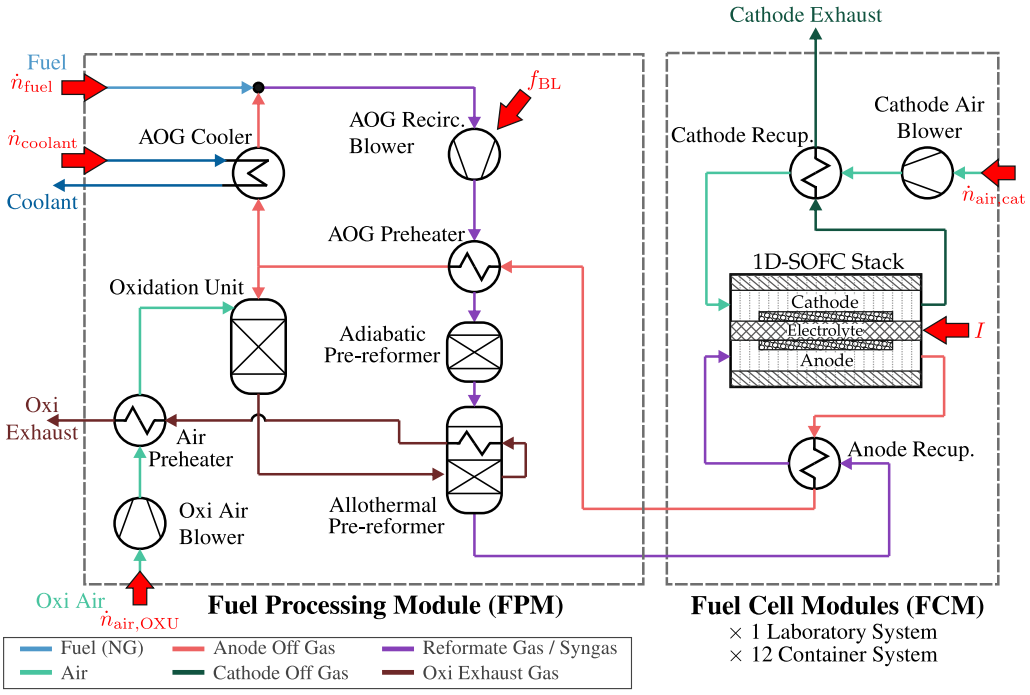

Figure 2. Overall plant layout, as presented in [7], consisting of one or multiple fuel cell modules (FCMs) and one fuel processing module (FPM). Manipulated system variables are indicated as red arrows.

In this study, a laboratory-scale SOFC system of this concept is investigated, consisting of one FCM with 720 planar electrolyte-supported cells and a corresponding FPM. The setup was already presented in [7] and delivers a rated electrical system net power of 15 kW. This system serves as a proof of concept for a scaled-up version for use in an intermodal container delivering an electrical net power of 300 kW. The layout of the scaled-up system is depicted in Figure 3 and consists of 12 FCMs in total. The centrally located FPM adapted in its size to handle the higher mass and heat flows provides the hydrogen-rich syn-gas to four horizontal branches (A–D), two of these branches placed one above the other, with three FCM each (e.g., A1–A3). The AOG mass flows are then mixed and fed back to the FPM according to Figure 2.

In contrast to conventional AOGR concepts with pre-reformers located in close proximity to the SOFC, the presented concept leads to significantly higher gas volumes in the anode recirculation loop affecting the transient operational behavior. The time delays between the FCMs and the FPM reach values in the order of seconds and might be different for individual FCMs, depending on their respective distance and pipe lengths to the FPM. With regard to the scaled-up system, individual FCM anode gas flows are not controllable but are subject to the actuation of the central recirculation blower and the branch mass flow distribution depending on the pressure drops of the parallel FCM branches. To successfully control such a system in a generally dynamic mode of operation within a constrained operating range, it is necessary to investigate in detail the gas flow interactions in the anode loop. These interactions are affected by chemical reactions, mass flow-dependent pressure drops, gas delay, and the actuation of fuel flow, electrical current, and blower speed. This study will focus on the laboratory-scale system, as the stack and BoP component characteristics were accessible at the time of publication and the control strategy based on this publication will be tested on this prototype first. A transfer to the scaled-up system will be conducted once the control scheme of the single FCM setup has proven successful.

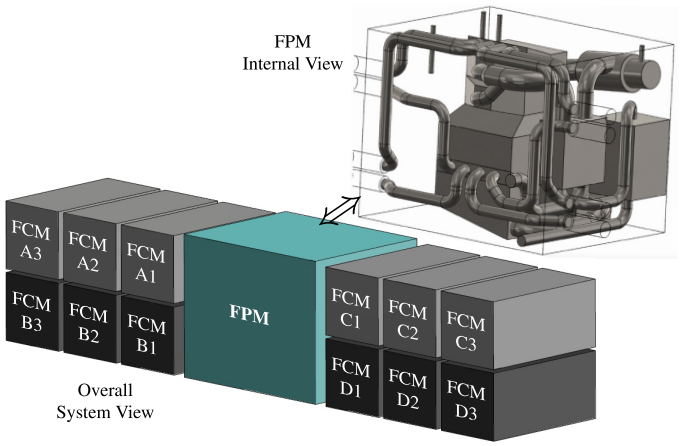

Figure 3. Scaled-up intermodal container system consisting of a central fuel processing module (FPM) and twelve fuel cell modules (FCM), arranged in four parallel branches of three modules each.

3. Modeling Methodology

The overall modeling approach is based on a first principle nonlinear state-space representation based on a set of differential-algebraic equations (DAEs) implemented in Matlab Simulink. The objective is to achieve the highest possible accuracy with the lowest possible computational effort. From a computational perspective, the simplest representation consists of lumped zero-dimensional models of the individual system components. These are based on energy and mass balance DAEs with additional quasi-static formulations regarding heat transfer or electrochemical reactions.

3.1. SOFC Stack Model

While this simplification is commonly used for control-oriented SOFC system modeling and especially for BoP components, it lacks accuracy with regard to the SOFC stack characteristics and reliable prediction of stack voltage and internal thermal gradients affecting the stack degradation. Due to the superposition of highly temperature-dependent transport mechanisms with the exothermic electrochemical redox reaction (ECR) and the strongly endothermic methane steam reforming (MSR), the distributions of temperature and the electrical current are closely coupled along the cell surface [19]. State-of-the-art models in the literature for planar co-flow or counter-flow cell designs thus utilize a one-dimensional discretization approach in the flow coordinate consisting of finite control volume segments. This method has proven to accurately depict the superimposed effects along the flow direction, as shown by segmented single-cell tests under realistic conditions [20]. However, one-dimensional modeling neglects the temperature profiles in the two remaining coordinates, mainly caused by heat transfer from the stack core to the colder lateral surfaces and the end plates of the stack. As heat losses increase, the accuracy of the one-dimensional model decreases due to oversimplified temperature and current density distributions.

The most prominent one-dimensional models include the publications from Braun [21] and Aguiar et al. [22], as well as more recent publications from Engelbracht [23] and van Biert et al. [24]. These models share a common set of model assumptions: a single-cell model is deployed and linearly extrapolated by the number of cells to depict the entire stack, thus neglecting a possible temperature distribution in the stacking coordinate. The temperature and gas distributions in the parallel gas channels are assumed to be uniform and perpendicular to the gas flow coordinate. A cascade of continuously stirred tank reactors (CSTRs) is utilized for species mass balancing in the anode and cathode channel control volumes. Regarding the temperature distribution, a set of four energy balances per control volume is used, two for solid material (cell and interconnect) and two for cathode and anode gas flow respectively. In all of the mentioned models, internal heat transfer is formulated by a conductive heat flow between two neighboring control volumes in the solid materials and a convective heat flow between the solids and the laminar gas flows of each control volume. The assumption of isopotential

electrode surfaces is made, resulting in a uniform cell voltage, which determines the spatial distribution of the electrical current. Finally, the electrochemical oxidation of CO is neglected, as the water–gas shift reaction (WGS) is considered the dominant reaction pathway, which is assumed to be in chemical equilibrium in each anode CSTR control volume.

However, the above-mentioned models differ with regard to the following aspects:

- **Electrochemical modeling:** Engelbracht used a lumped area-specific resistance (ASR) approach to quantify the local voltage losses in each control volume, whereas the other models differentiate between ohmic, activation, and concentration overpotentials, thus, if parameterized correctly, yielding a physically more accurate model, yet with significantly higher computational effort. The ASR assumption that an overall resistance depends only on temperature, resulting in a linear current–voltage characteristic, could be experimentally confirmed with a planar short-stack up to a stack fuel utilization of $FU_{\text{stack}} = 80\%$ [25]. However, using this simplified approach may result in deviations at (i) higher fuel or air utilization, due to the neglect of mass transport phenomena, and (ii) cells with a higher proportion of activation overpotentials, which does not occur in this simulation study.
- **Heat transfer mechanisms:** Braun and Aguiar et al. considered radiation heat transfer between the cell and interconnects in each control volume as a third heat flow path, whereas Engelbracht and van Biert et al. neglect the effect of radiation arguing that local temperature differences of cell and interconnect in each control volume are small in planar cell designs. Moreover, van Biert further expanded the cell model by adding additional chemically inactive control volumes upstream and downstream. This was done to depict the manifold, converge the gas inlet temperatures, and assign the heat losses to the surrounding environment. In contrast, the other models either neglect heat losses or distribute them uniformly across all cell control volumes.
- **Reaction kinetics:** The spatial distribution of MSR is considered a significant factor in the overall cell behavior due to its endothermic nature at the inlet section of the anode. A widely used approach is a first-order MSR kinetic model proposed by Achenbach [26], which is also used by Braun and Aguilar et al. depending on the temperature and CH_4 partial pressure. Moreover, van Biert compared a set of MSR kinetic models with regard to the overall stack characteristics and identified a Langmuir–Hinshelwood approach to be the best fit based on the evaluation of direct internal reforming experiments in a realistic single-cell setup [27].

In order to obtain an accurate plant model for dynamic system analysis, a one-dimensional stack model close to the variant of van Biert is chosen, as the investigated stacks in the laboratory-scale system are almost identical to the stack from the cell manufacturer Sunfire GmbH experimentally validated in [24]. Figure 4 illustrates the discretization of the chosen model layout in the flow direction as well as the underlying assumptions of heat loss distribution to the manifolds, the periodic boundary condition at the interconnects, the neglect of radiation as a heat transfer phenomenon inside the stack, as well as using the more advanced Langmuir–Hinshelwood MSR reaction kinetics model. However, the ASR approach from Engelbracht is chosen as it represents a suitable simplification for electrolyte-supported cells in the targeted fuel utilization range. Furthermore, parameterization of the electrochemical model is possible by means of experimental single-cell measurements. The active cell area in this publication is divided into 20 control volumes with 8 + 8 chemically inactive manifold control volumes upstream and downstream which was found to represent a good compromise between accuracy and computation time.

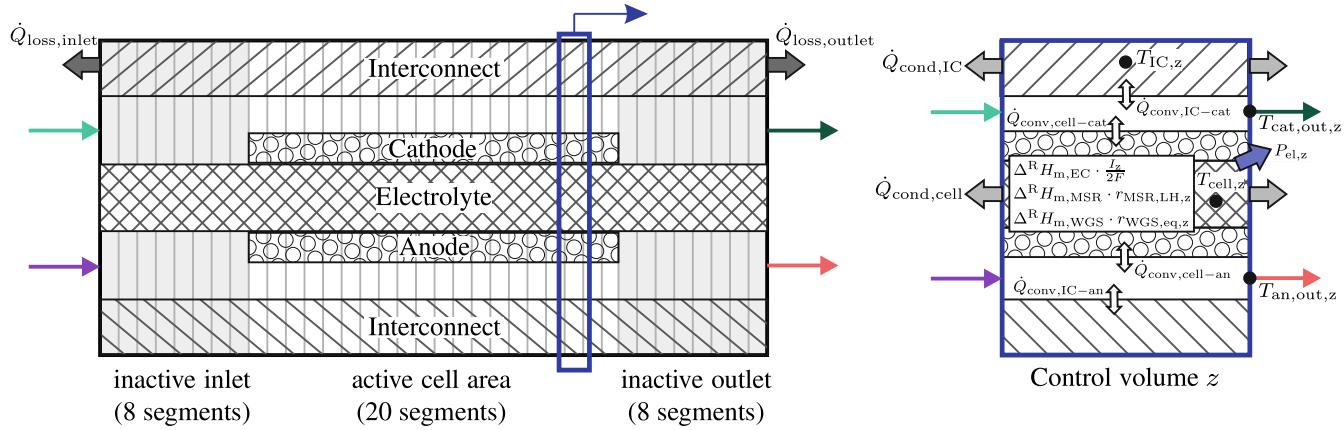

Figure 4. SOFC Stack model layout. Left: discretization into control volumes in the flow direction. Right: close-up of one control volume.

3.2. Balance of Plant (BoP) Component Models

BoP component modeling in the literature mainly varies in terms of the degree of component discretization, consideration of pressure drops, heat losses, and gas delays, as well as in the approach used to determine the amount of recirculated off-gas.

Engelbracht [23] chose to discretize all major BoP components, such as the allothermal pre-reformer and afterburner, as a cascade of CSTRs similar to his approach with SOFCs, while Stiller only [14] discretized the heat exchangers in order to capture their dynamic thermal characteristics. Other authors, like Carré [12], Braun [21], and Kupecki [18], used a lumped approach for all BoP components. A distinct feature of Stiller's model is the consideration of gas transport delays in between the lumped model components to account for the gas residence times. This is realized by adiabatic pipes with time delays determined by component volume and the ideal gas law. Heat losses apart from the SOFC stack are neglected in all models, except for those by Carré, either by simplification or the assumption of a high level of module integration. Pressure drops of the gas flows are considered to estimate the required electric power from the blowers affecting the system's net efficiency. However, the pressure drop calculation in the anode loop is typically not utilized to determine the share of recirculated gas, as the recirculation ratio is taken as a plant input variable. On the contrary, Kupecki implemented the performance map of the recirculation blower in order to determine the required electric rotational blower frequency $f_{\mathrm{bl,rec}}$ as a function of the anode loop pressure drop and the recirculating mass flow $\Delta p_{\mathrm{bl,rec}} = f(\dot{m}_{\mathrm{bl,rec}}, f_{\mathrm{bl,rec}})$ for stationary system simulation.

This publication aims to merge the above-mentioned model approaches to adequately depict the dynamic behavior of the targeted plant model. BoP components are implemented as lumped zero-dimensional models in order to decrease computational effort. This simplification is supported by the previous experimental characterization of the heat exchangers, a grid independence study on heat transfer, and the degree of pre-reforming in the allothermal pre-reformer, as well as the implementation of corresponding heat transfer correlations [7]. Heat losses are considered in all BoP components as they have been determined in detail by means of a steady-state thermal analysis, considering the individual component insulation.

The spatial separation of the fuel cell stack modules from the central FPM represents a novelty compared to published system designs. This new design, dictated by ship construction boundary conditions, inevitably leads to higher gas volumes in the anode gas loop heavily affecting the transient system behavior. Therefore, this publication places considerable emphasis on the correct dynamic representation of the gas residence times following the approach of Stiller.

In order to achieve a realistic dynamic depiction of the AOG mass flow distribution, the operating characteristics of the recirculation blower need to be implemented according to the approach of Kupecki, as the blower represents the flow-determining component. Due to the closed loop structure, the overall component pressure drops in the loop are imposed

on the blower to be overcome, which, together with a given rotational speed, results in the mass flow conveyed by the blower. This in turn defines the amount of recirculated AOG, thus the recirculation ratio RR. Implementation of the blower characteristics into the plant model is also beneficial with regard to system control to estimate the state of recirculation without directly measuring the hot mass flow in the anode loop, as such sensors are considered cost-intensive and prone to failure [16,28].

In contrast, setting the inlet air mass flows at ambient temperature to their desired set points can be considered as a straightforward subordinate and independent control task, as mass flow meters in the immediate vicinity of the blowers are implemented to set the blower frequencies accordingly. It is assumed that the mass flows are set to their respective set point without significant control delay at all times so that these blower characteristics do not have to be considered and the blowers are only modeled in terms of their power demand and the rise in air temperature. Analogously, ideal control of the gaseous fuel mass flow is assumed with the aid of a conventional mass flow controller.

3.3. Governing Equations

Each component depicted inside the system boundaries in Figure 2 is modeled using a set of the following equations stated with the associating assumptions. An overview is given in Table 1. The fuel flow, treated as pure CH_4, and the dry air flows enter the system at ambient conditions ($T_{amb} = 25\,°C$, $p_{amb} = 1\,bar$). Co-generation of useful heat in downstream exhaust gas heat exchangers is not considered in this study.

Table 1. Overview of deployed equations inside the component models.

Component Name	M	E	EC	Δp	Δt
SOFC Stack	$2 \times N_{CV,act}$	$4 \times N_{CV,tot}$	$1 \times N_{CV,act}$	2×	2×
Allothermal pre-reformer	1×	2×	–	2×	2×
Adiabatic pre-reformer	1×	1×	–	1×	1×
Heat exchanger	–	2×	–	2×	2×
Oxidation unit	1×	1×	–	1×	1×

Conservation of mass, including chemical reactions M: For each species, i, present in the respective flow, a DAE is formulated using the ideal gas law rearranged to the molar fraction x_i, which is equal to the outlet molar fraction $x_{i,out}$ in a CSTR [12]:

$$\frac{dx_{i,out}}{dt} = \frac{R_m \cdot T_{out}}{p \cdot V}\left(x_{i,in}\dot{n}_{in} - x_{i,out} \cdot \left(\dot{n}_{in} + \sum_k \sum_i \nu_{i,k} \cdot r_k\right) + \sum_k \nu_{i,k} \cdot r_k\right),$$

with $x_{i,in}$ and $\dot{n}_{in}$ being the inlet molar fraction and overall molar flow, considering a total of k reactions occurring simultaneously with the corresponding stoichiometric coefficients $\nu_{i,k}$ and reaction rates r_k. In accordance with models in the literature, this formulation implies the assumption of a quasi-static total outlet molar flow. This assumption is permissible due to the high prevailing temperatures and significant thermal inertia of the components; see [12,24].

At the SOFC cathode, molecular oxygen is reduced to oxygen ions (ORRs), which mitigate through the electrolyte and lead to the oxidation of hydrogen (HOR) at the anode, resulting in the net electrochemical reaction and an associated electron flow:

$$O_2 + 2\,e^- \longrightarrow O^{2-} \quad \text{(ORR)}, \tag{4}$$

$$H_2 + O^{2-} \longrightarrow H_2O + 2\,e^- \quad \text{(HOR)}, \tag{5}$$

$$H_2 + \frac{1}{2}O_2 \longrightarrow H_2O \quad \text{(ECR)}. \tag{6}$$

The ORR and HOR reaction rates of the associated species are, thus, related to the local current density determined by the EC submodule. The MSR and WGS reactions occur at the SOFC anode and in the pre-reforming reactors:

$$\mathrm{CH_4 + H_2O \rightleftharpoons CO + 3\,H_2} \quad \text{(MSR)}, \tag{7}$$

$$\mathrm{CO + H_2O \rightleftharpoons CO_2 + H_2} \quad \text{(WGS)}. \tag{8}$$

Reaction rate modeling differs with respect to the associated component assumptions. The WGS reaction is assumed to be in equilibrium, both in the SOFC control volumes and lumped pre-reformers. Formulating the sum of the forward and backward reaction rates and inserting the equilibrium constant $K_{\mathrm{eq,WGS}} := k_{\mathrm{WGS,f}}/k_{\mathrm{WGS,b}}$ yields [29]:

$$r_{\mathrm{WGS}} = k_{\mathrm{WGS,b}} \cdot \left(K_{\mathrm{eq,WGS}}(T)\, p_{\mathrm{CO,out}}\, p_{\mathrm{H_2O,out}} - p_{\mathrm{CO_2,out}}\, p_{\mathrm{H_2,out}}\right), \tag{9}$$

with $k_{\mathrm{WGS,b}}$ being the backward reaction rate constant and $p_{i,\mathrm{out}}$ the CSTR partial pressure of species i. The equilibrium constant can be calculated by means of the standard molar Gibbs enthalpy of the WGS reaction:

$$K_{\mathrm{eq,WGS}}(T) = \exp\left(\frac{-\Delta^{\mathrm{R}} G^{\Theta}_{\mathrm{m,WGS}}(T)}{R_{\mathrm{m}} \cdot T}\right). \tag{10}$$

Regarding the MSR reaction rate in the pre-reformers, chemical equilibrium is assumed due to the high activity of the used precious metal catalyst and the high gas residence times. Thus, a similar expression for the MSR equilibrium reaction rate is formulated:

$$r_{\mathrm{MSR,eq}} = k_{\mathrm{MSR,b}} \cdot \left(K_{\mathrm{eq,MSR}}(T)\, p_{\mathrm{CH_4,out}}\, p_{\mathrm{H_2O,out}} - p^3_{\mathrm{H_2,out}}\, p_{\mathrm{CO,out}}\right). \tag{11}$$

The values of the backward reaction rate constants $k_{\mathrm{WGS,b}}$ and $k_{\mathrm{MSR,b}}$ are only of numerical significance and should be chosen large enough for the correct calculation of equilibrium composition [29]. However, too large values lead to an increased computational effort. Thus, a sensitivity study of the backward reaction rate constants was performed for each equilibrium reaction in both the pre-reformers and the stack. A trade-off was achieved by setting the backward reaction rate constants for each reactor to the values depicted in Table 2, which leads to a maximum absolute molar composition error of 0.2 mol-% in the investigated operating range.

In contrast, the area-specific kinetic Langmuir–Hinshelwood approach from van Biert et al. [24] is used for each discretized anode control volume:

$$\begin{aligned} r_{\mathrm{MSR,LH}} = k_{0,\mathrm{MSR}} \cdot \exp\left(\frac{-E_{\mathrm{act,MSR}}}{R_{\mathrm{m}} T}\right) \cdot \frac{p_{\mathrm{CH_4,out}}}{\left(1 + K_{\mathrm{CH_4}} p_{\mathrm{CH_4,out}} + K_{\mathrm{H_2O}} \frac{p_{\mathrm{H_2O,out}}}{p_{\mathrm{H_2,out}}}\right)^2} \\ \cdot \left(1 - \frac{1}{K_{\mathrm{eq,MSR}}(T)} \frac{p_{\mathrm{CO,out}} p^3_{\mathrm{H_2,out}}}{p_{\mathrm{CH_4,out}} p_{\mathrm{H_2O,out}}}\right) \cdot \frac{A_{\mathrm{cell}}}{N_{\mathrm{CV,act}}}. \end{aligned} \tag{12}$$

The values of the pre-exponential factor $k_{0,\mathrm{MSR}}$, the activation energy $E_{\mathrm{act,MSR}}$, as well as the adsorption constants $K_{\mathrm{CH_4}}$ and $K_{\mathrm{H_2O}}$ are directly adopted from [27], whereas $K_{\mathrm{eq,MSR}}(T)$ is calculated analogously to Equation (10). At the oxidation unit, a total conversion of the remaining combustible AOG species is assumed so that the reaction rates are determined by the respective molar flows:

$$\mathrm{H_2} + \frac{1}{2}\,\mathrm{O_2} \longrightarrow \mathrm{H_2O} \quad (\mathrm{H_2\ comb.})\ , \tag{13}$$

$$\mathrm{CO} + \frac{1}{2}\,\mathrm{O_2} \longrightarrow \mathrm{CO_2} \quad (\mathrm{CO\ comb.})\ , \tag{14}$$

$$\mathrm{CH_4} + 2\,\mathrm{O_2} \longrightarrow \mathrm{CO_2} + 2\,\mathrm{H_2O} \quad (\mathrm{CH_4\ comb.}). \tag{15}$$

Conservation of Energy, including chemical reactions E: The general energy balance DAE is shown in Equation (16), considering enthalpy changes of fluids entering

and leaving as ideal gases, as well as reaction enthalpies, heat flows $\dot{Q}_i$, and electrical or mechanical power P_i:

$$\frac{\mathrm{d}T_{\mathrm{out}}}{\mathrm{d}t} = \frac{1}{m \cdot c_{\mathrm{p}}(T)} \Bigg(\sum_i \dot{n}_{i,\mathrm{in}} \cdot \int_{T_0}^{T_{\mathrm{in}}} C_{\mathrm{m,p},i}(T)\,\mathrm{d}T - \sum_i \dot{n}_{i,\mathrm{out}} \cdot \int_{T_0}^{T_{\mathrm{out}}} C_{\mathrm{m,p},i}(T)\,\mathrm{d}T - \sum_k \Delta^{\mathrm{R}} H_{\mathrm{m},k}(T_0) \cdot r_k + \sum_i \dot{Q}_i + \sum_i P_i \Bigg), \tag{16}$$

where T_{out} is the lumped temperature according to the CSTR assumption, m is the mass of the component under consideration and c_{p} its specific heat capacity. $C_{\mathrm{m,p},i}$ represents the temperature-dependent molar isobaric heat capacity of the corresponding ideal gas mixture and $\Delta^{\mathrm{R}} H_{\mathrm{m},k}(T_0)$ is the molar reaction enthalpy of reaction k at reference temperature $T_0 = 1000\,\mathrm{K}$.

According to the lumped model assumption, BoP components comprise one energy DEA per fluid stream, as depicted in Table 1. Thus, it is assumed that the fluids leave at the solid component temperature, which couples the thermal gas behavior with the dominating thermal inertia of the solid. For components with two fluid streams, the masses are distributed among the two balance equations with respect to the fluid's degree of component interaction. For plate-fin heat exchangers, the mass is distributed uniformly to the DAEs, whereas for shell-and-tube heat exchangers, including the allothermal pre-reformer, both the mass of the shell and half of the mass of the tube are assigned to the hot shell flow due to the larger heat transfer surface.

Regarding the discretized stack, the four energy DAEs per control volume are formulated for the gas temperatures $T_{\mathrm{an,out}}$ and $T_{\mathrm{cat,out}}$, the solid temperatures of the overall cell T_{cell}, and the interconnect T_{ic} identical to [24]. Heat is generated through reaction in the cell, and heat conduction between two neighboring spatial solid control volumes occurs in accordance with Fourier's law, governed by the solid thermal conductivity of the cell and the interconnect. Four convective heat flows occur per control volume between the solid–fluid pairs ($\dot{Q}_{\mathrm{conv,cell-an}}$, $\dot{Q}_{\mathrm{conv,cell-cat}}$, $\dot{Q}_{\mathrm{conv,ic-an}}$, $\dot{Q}_{\mathrm{conv,ic-cat}}$), and are expressed in the following form:

$$\dot{Q}_{\mathrm{conv,s-g}} = h \cdot A \cdot \left(T_{\mathrm{g,out}} - T_{\mathrm{s}}\right) \quad \text{, with} \quad h = \frac{\mathrm{Nu} \cdot \lambda(T, \vec{x})}{d_{\mathrm{hyd,ch}}} \tag{17}$$

as the local heat transfer coefficient, depending on the Nusselt number Nu, the thermal conductivity of the respective fluid λ, and the hydraulic channel diameter $d_{\mathrm{hyd,ch}}$. In alignment with the authors' concerns regarding stack modeling mentioned above, a constant value of 3.09 is chosen for the Nusselt number due to a fully developed rectangular laminar channel flow.

Heat transfer in the BoP heat exchangers is modeled using the NTU method by calculating the maximum possible heat flow and scaling it with the heat exchange effectiveness ϵ [30]:

$$\dot{Q}_{\mathrm{HEX}} = \dot{Q}_{\mathrm{HEX,max}} \cdot \epsilon(UA). \tag{18}$$

Apart from the flow configuration and the fluid's heat capacity rates, the effectiveness depends on the overall heat transfer coefficient U, determined by the convective heat transfer on the cold and hot sides $h_{\mathrm{c/h}}$, as well as the thermal wall conduction resistance:

$$UA = \left(\frac{1}{h_{\mathrm{c}} A_{\mathrm{c}}} + R_{\mathrm{wall}} + \frac{1}{h_{\mathrm{h}} A_{\mathrm{h}}} \right)^{-1}. \tag{19}$$

Nusselt correlations for the implemented heat exchangers in the form $\mathrm{Nu} = f(\mathrm{Re}, \mathrm{Pr})$ were determined experimentally and are documented in [7]. Heat losses in all BoP components, as well as the outer interconnect DAEs of the stack model, are implemented analogously to Equation (17):

$$\dot{Q}_{\mathrm{loss},i} = (h \cdot A)_{\mathrm{loss}} \cdot (T - T_{\mathrm{amb}}). \tag{20}$$

Heat loss transfer coefficients are parameterized according to the thermal simulation results of the individual components.

Electrochemical Modeling EC:

For each active cell control volume identified by the spatial index z, the local voltage losses and electric current are determined with the quasi-static voltage breakdown:

$$U_{\text{cell},z} = U_{\text{cell},0,z}(T_{\text{cell},z}, \vec{x}_z) - ASR(T_{\text{cell},z}) \cdot \frac{I_z}{A_{\text{cell}}/N_{\text{CV,act}}}, \tag{21}$$

using the local Nernst potential, depending on temperature and the molar fractions of reactants:

$$U_{\text{cell},0,z}(T_{\text{cell},z}, \vec{x}_z) = -\frac{\Delta^{\text{R}} G_{\text{m}}^{\Theta}(T_{\text{cell},z})}{2F} - \frac{R_{\text{m}} \cdot T_{\text{cell},z}}{2F} \cdot \ln\left(\frac{x_{\text{an},z,\text{H}_2\text{O}}}{x_{\text{an},z,\text{H}_2} \cdot x_{\text{cat},z,\text{O}_2}^{0.5}}\right). \tag{22}$$

The overall ASR is typically formulated as an Arrhenius type to address the dominating temperature-dependent ionic conductivity in the electrolyte [23]. The equation is expanded by a linear degradation rate $\text{d}ASR$ given in $\text{m}\Omega\,\text{cm}^2\,\text{kh}^{-1}$ provided by the cell manufacturer [31] to account for degraded cell operation after a specific operating time t_{op} in hours:

$$ASR(T, t_{\text{op}}) = \left(ASR_{\text{ref}} + \text{d}ASR \cdot \frac{t_{\text{op}}}{1000}\right) \cdot \exp\left[\frac{E_{\text{act,ASR}} \cdot F}{R_{\text{m}}}\left(\frac{1}{T} - \frac{1}{T_{\text{ref}}}\right)\right] + ASR_{\text{c}} \tag{23}$$

The reference ASR at the reference temperature T_{ref} and begin of life, the activation energy $E_{\text{a,ASR}}$, as well as the offset contact resistance ASR_{c} were determined experimentally by evaluation of polarization curves from a single cell in a high-temperature test bench and are given in Table 2. The test setup and the experimental operating procedure are explained in detail in [32]. Coupling the electrochemical equations of each active control volume is realized by means of the following algebraic constraints to set the requested cell current I and the isopotential boundary condition:

$$\sum_{z=1}^{N_{\text{CV,act}}} I_z = I \quad \text{and} \quad U_{\text{cell},z} = U_{\text{cell}} \quad \forall z \in [1, N_{\text{CV,act}}]. \tag{24}$$

Finally, the overall electrical stack power is determined by linearly extrapolating the single-cell behavior:

$$\left|P_{\text{el,SOFC,DC}}\right| = U_{\text{cell}} \cdot N_{\text{cell}} \cdot I. \tag{25}$$

Gas residence time Δt:

Following the pipe modeling of Stiller, the time delay associated with the respective component and pipe volumes are calculated by means of the ideal gas law:

$$\Delta t_i = \frac{p_i \cdot V_i}{R_{\text{m}} \cdot \dot{n}_i \cdot T_i}, \tag{26}$$

considering the component volume V_i filled with gas at temperature T_i and pressure p_i at a molar flow rate $\dot{n}_i$. To avoid an unnecessary number of consecutive gas delays, volumes of adjacent pipes and components are merged into one without sacrificing modeling details.

Laminar pressure drop Δp:

As a rough approximation, laminar pipe flow is assumed in all components enabling the use of the Hagen–Poiseuille equation, depending on gas density ρ, flow velocity w, geometry, and the Reynolds number Re. By inserting the definition of the Reynolds number, a linear dependence on the mass flow $\dot{m}_i$ is obtained:

$$\Delta p_{\text{lam},i} = \frac{1}{2}\rho\, w^2 \frac{l}{D}\frac{64}{\text{Re}} = k_{\text{p},i} \cdot \dot{m}_i \cdot \frac{\eta(T_i, \vec{x}_i)}{\rho(p_i, T_i, \vec{x}_i)}, \tag{27}$$

depending on the dynamic viscosity η, density ρ, and the pressure loss coefficient $k_{p,i}$. Values for $k_{p,i}$ are assigned based on the individual component design nominal pressure drops, which were chosen to reach the maximum anode overpressure of 50 mbar at maximum electrical current and begin of life to avoid unnecessary high BoP power demand.

The thermodynamic behavior of all implemented blowers is based on an ideal gas isentropic pressure change from $p_{bl,in}$ and $T_{bl,in}$ to the desired outlet pressure $p_{bl,out}$ complemented by the isentropic efficiency $\eta_{bl,is}$ yielding the blower outlet temperature:

$$T_{bl,out} = T_{bl,in} + \frac{T_{bl,in}}{\eta_{bl,is}} \left(\left(\frac{p_{bl,out}}{p_{bl,in}} \right)^{\frac{R_m}{C_{m,p}}} - 1 \right). \tag{28}$$

Electrical power demand is modeled by using the corresponding enthalpy difference and considering a mechanical blower efficiency $\eta_{bl,mech}$ accounting for friction and electric motor irreversibilities:

$$P_{el,bl} = \frac{1}{\eta_{bl,mech}} \cdot \dot{n}_{bl} \cdot \left(H_{m,out}(T_{bl,out}, \vec{x}_{bl}) - H_{m,in}(T_{bl,in}, \vec{x}_{bl}) \right). \tag{29}$$

Regarding the recirculation blower, the operating map of the implemented side channel blower is utilized, which relates the mass flow with the imposed pressure drop of the anode loop and a specified electrical blower rotation frequency $f_{bl,rec}$:

$$\dot{n}_{bl,rec} = \frac{1}{M_{bl,rec}} \cdot \dot{m}_{bl,rec}(\Delta p_{bl,rec}, f_{bl,rec}) \quad \text{, with} \quad \Delta p_{bl,rec} = \sum_i \Delta p_{lam,AOGR,i}. \tag{30}$$

The recirculation ratio is, thus, determined by the blower characteristics and the molar fuel flow:

$$RR := \frac{\dot{n}_{AOG,rec}}{\dot{n}_{AOG,total}} \cdot 100\% = \frac{\dot{n}_{bl,rec} - \dot{n}_{fuel}}{\dot{n}_{AOG,total}} \cdot 100\%. \tag{31}$$

Finally, the system electrical net power is calculated by subtracting the BoP blower power demand (Equation (29)) from the SOFC power output (Equation (25)):

$$P_{el,net} = |P_{el,SOFC,DC}| \cdot \eta_{pe} - (P_{el,bl,ca} + P_{el,bl,rec} + P_{el,bl,oxi}), \tag{32}$$

considering a generalized efficiency of the SOFC power electronics η_{pe}. The system's net efficiency rates the net power with the lower heating value of supplied fuel:

$$\eta_{sys,net} = \frac{P_{el,net}}{\dot{n}_{fuel} \cdot LHV_{fuel}}. \tag{33}$$

Table 2. Selected SOFC and BoP parameters.

Parameter	Value	Unit
SOFC Stack geometry and thermophysical properties, taken from [24]		
Number of cells N_{cell}	720	-
Number of active SOFC control volumes $N_{CV,act}$	20	-
Number of total SOFC control volumes $N_{CV,tot}$	36	-
Cell length L_{cell}	0.164	m
Active cell length L_{act}	0.09	m
Cell width w_{cell}	0.142	m
Active cell area $A_{cell} = L_{act} \cdot w_{cell}$	127.8	cm^2
Interconnect thickness δ_{IC}	0.0005	m
Channel height δ_{ch}	0.001	m
Hydraulic channel diameter $d_{hyd,ch}$	0.0017	m
Thermal conductivity of cell λ_{cell}	2	$W\,m^{-1}\,K^{-1}$
Thermal conductivity of interconnect λ_{IC}	24	$W\,m^{-1}\,K^{-1}$

Table 2. *Cont.*

Parameter	Value	Unit
SOFC Electrochemical Data obtained from single-cell measurements		
ASR at reference temperature ASR_{ref}	0.2681	$\Omega\,\mathrm{cm}^2$
ASR offset contact resistance ASR_{c}	0.189	$\Omega\,\mathrm{cm}^2$
ASR reference temperature T_{ref}	1133.15	K
ASR activation energy $E_{\mathrm{act,ASR}}$	1.05	eV
ASR degradation rate dASR	0.015	$\Omega\,\mathrm{cm}^2\,\mathrm{kh}^{-1}$
Equilibrium backward reaction rate constants		
WGS in adiab. pre-reformer $k_{\mathrm{WGS,adRef,b}}$	2.7	-
WGS in allotherm. pre-reformer $k_{\mathrm{WGS,allRef,b}}$	0.18	-
WGS in SOFC $k_{\mathrm{WGS,SOFC,b}}$	20	-
MSR in adiab. pre-reformer $k_{\mathrm{MSR,adRef,b}}$	3200	-
MSR in allotherm. pre-reformer $k_{\mathrm{MSR,allRef,b}}$	800	-
BoP Component efficiencies, analogous to [7]		
Isentropic blower efficiency $\eta_{\mathrm{bl,is}}$	70	%
Mechanical blower efficiency $\eta_{\mathrm{bl,mech}}$	80	%
Power electronics efficiency η_{pe}	95	%

3.4. Thermophysical Data

Thermodynamic properties of pure gaseous species, namely the molar isobaric heat capacity $C_{\mathrm{m,p},i}(T)$, thermal conductivity $\lambda_i(T)$ and dynamic viscosity $\eta_i(T)$, are modeled as a function of temperature using deducted lower-degree functions of NASA Polynomials [33] for the relevant temperature range between 25 °C and 900 °C. To reduce the computational effort, a linear fit is used by default, unless the maximum relative deviation exceeds a value of 2 %, in which case, a quadratic fit is used. Corresponding data are listed in Appendix A. Molar heat capacities of the multi-component gas mixtures are calculated assuming ideal gas mixtures:

$$C_{\mathrm{m,p}}(T,\vec{x}) = \sum_i x_i \cdot C_{\mathrm{m,p},i}(T), \tag{34}$$

while for thermal conductivity and dynamic viscosity, the mixing methods of Wilke [34] and Mason and Saxena [35] are utilized respectively. Gas mixture density is calculated by means of the ideal gas law:

$$\rho(p,T,\vec{x}) = \frac{p \cdot \bar{M}(\vec{x})}{R_{\mathrm{m}} \cdot T} \quad \text{, with} \quad \bar{M}(\vec{x}) = \sum_i x_i \cdot M_i \tag{35}$$

being the average molar mass of the gas mixture. Molar Gibbs reaction enthalpies at standard pressure $\Delta^{\mathrm{R}}G^{\Theta}_{\mathrm{m}}(T)$ required both for the electrochemical calculation (Equation (22)) and determination of MSR and WGS equilibrium constants (Equation (10)) are modeled by linear temperature fits originating from the NASA polynomial enthalpies and entropies of the pure species according to the respective reaction:

$$\begin{aligned} \Delta^{\mathrm{R}}G^{\Theta}_{\mathrm{m}}(T) = \Delta^{\mathrm{R}}H^{\Theta}_{\mathrm{m}}(T) - T \cdot \Delta^{\mathrm{R}}S^{\Theta}_{\mathrm{m}}(T), \quad \text{with} \quad \Delta^{\mathrm{R}}H^{\Theta}_{\mathrm{m}}(T) = \sum_i \nu_i \cdot H_{\mathrm{m},i}(T) \\ \text{and} \quad \Delta^{\mathrm{R}}S^{\Theta}_{\mathrm{m}}(T) = \sum_i \nu_i \cdot S_{\mathrm{m},i}(T) \end{aligned} \tag{36}$$

and are given in Appendix A. The specific heat capacities of the solids for calculating the thermal inertia, namely 1.4828 stainless steel as a default BoP material and aluminum oxide as the main catalyst material, are also approximated as polynomial functions (see Appendix B), while the overall thermal inertia of the FCM was experimentally obtained by heating-up curves.

3.5. Operating Limitations

The system operation is constrained by the following system parameters:

- **Oxygen utilization OU_{stack}**: Thermal management of the SOFC stack by means of excess airflow is constrained by the availability of oxygen molecules for ORR. In this study, a maximum oxygen utilization of $OU_{\text{stack,max}} = 40\,\%$ is set to prohibit oxygen starvation at the reaction layer and to remain in the validity range of the *ASR* approach. As a result, the maximum target stack temperature of 860 °C is not reached in the partial load range.
- **Fuel utilization FU_{stack}**: Low hydrogen-to-steam ratios, which typically occur at anode outlets at high fuel utilizations, favor the thermochemical oxidation of the Ni catalyst, which represents a significant degradation mechanism [36]. Fuel utilization is, thus, constrained to a conservative steady-state value of $FU_{\text{stack,max}} = 75\,\%$, allowing for small overshoots to up to 80 % during transient operation.
- **Cell voltage: U_{cell}**: Electrochemical oxidation of Ni is favored at cell voltages below 0.7 V at 800 °C, but is considered less dominant than thermochemical oxidation at non-extreme fuel utilizations [36]. The lowest permissible cell voltage is, therefore, set to a value of $U_{\text{cell,min}} = 0.65\,\text{V}$.
- **Anode overpressure: p_{an}**: A maximum of $p_{\text{an,max}} = 50\,\text{mbar}$ above ambient pressure at the anode inlet is set to avoid possible leakage from the anode to the surroundings.
- **Oxygen-to-carbon ratio *O*/*C***: Carbon formation is most likely to occur at the catalyst in the adiabatic pre-reformer. To estimate the risk of carbon formation, thermodynamic equilibrium data provided by Jaworski et al. [37] in the form of equilibrium threshold lines in a ternary C/H/O diagram are utilized. Two exemplary threshold lines from this publication at atmospheric pressure at 400 °C and 800 °C are depicted as solid blue and red lines in the ternary plot in Figure 5 left. A lower O/C limit for each temperature is estimated by the determination of the O/C iso-line that just touches the threshold line in one point. By this, a worst-case estimation independent from the actual gas composition is achieved. Figure 5 right shows the derived values for the seven given temperatures depicted as filled squares and a fifth-order polynomial fit given in Appendix C. For the plant model, the temperature of the adiabatic pre-reformer is then used to determine the lower limit $O/C_{\text{min}} = f(T_{\text{adRef,out}})$.

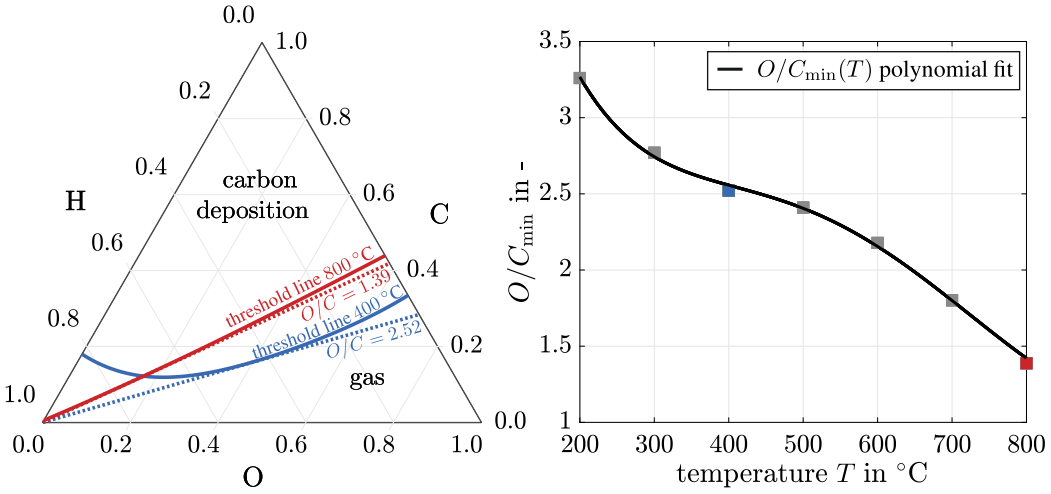

Figure 5. Determination of O/C_{min}. Left: Ternary C/H/O diagram and two exemplary threshold lines at 400 °C and 800 °C for carbon deposition at atmospheric pressure taken from [37] along with corresponding lines of constant O/C. Right: deducted O/C_{min} values as a function of temperature (filled squares) and corresponding polynomial fit.

In order to graphically represent the SOFC system operating map together with the above-mentioned constraints, the system fuel utilization FU_{sys} is plotted against the

recirculation ratio RR, see Figure 6 left. By using Equations (2) and (3), lines of constant FU_{stack} and O/C are added as dashed and dotted lines, respectively. To serve as an illustration, the right figure shows four exemplary constraint lines regarding the anode loop ($FU_{\text{stack,max}}$, $O/C_{\text{min}}(T_{\text{adRef,out}})$, $U_{\text{cell,min}}$, $p_{\text{an,max}}$) that enclose the valid operating range depicted in green.

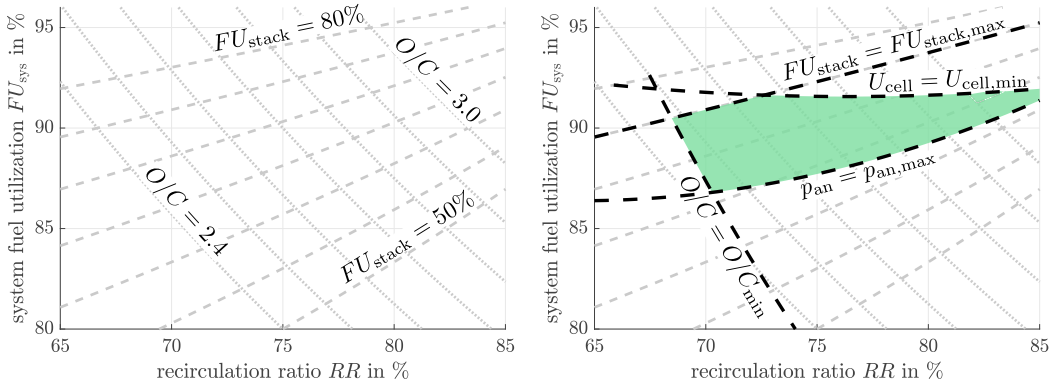

Figure 6. Concept of stationary operating maps at constant electrical current. Left: Dashed lines of constant FU_{stack} in 5 %-point increments and dotted lines of constant O/C in 0.1 increments. Right: Exemplary limiting lines and permissible operating range depicted as filled green area.

4. Steady-State Simulation Results

4.1. Spatially Distributed SOFC Model

In the first step, the steady-state full and partial load behavior of the single FCM at constant inlet conditions is investigated to depict the stack behavior independent from the thermal BoP pre-reforming capability. The inlet conditions are given in Table 3 and represent conditions derived from full-load system operations at typical heat recuperation temperatures. The gas composition corresponds to a pre-reformed syngas at $FU_{\text{stack}} = 75\,\%$ and $RR = 70\,\%$, giving a O/C ratio of 2.54. The airflow is controlled to maintain a maximum cell temperature of 860 °C as long as oxygen utilization is below its limit. The simulation results for five electrical currents varied in the range of 15 A and 35 A in 5 A increments, as shown in Figure 7. The first three figures depict the distribution of electrical current density $i(z)$, cell temperature $T_{\text{cell}}(z)$, and its spatial gradient $\mathrm{d}T_{\text{cell}}/\mathrm{d}z$ along the normalized flow coordinate z with the gases passing in a co-flow configuration from left to right. The bottom right plot shows the corresponding cell voltage and stack oxygen utilization as well as the threshold electrical current of 20 A, below which the cathode molar flow cannot be decreased enough in terms of stack temperature control due to $OU_{\text{stack,max}}$ limitation. As a consequence, the cell temperature profile at 15 A in Figure 7b does not reach the desired maximum target value.

The cell temperatures are characterized by a local minimum caused by the endothermic MSR reaction at the inlet region of the active cell area and a local maximum at the outlet region followed by a temperature decline due to the heat loss at the outlet manifold. These effects are also reported in co-flow stack simulation publications using direct internal reforming [19,24] and, thus, confirm reasonably accurate modeling of the stack interactions required for estimating the thermal gradients.

Table 3. Inlet conditions for stack simulations.

Operating Parameter			Value	Unit
Anode inlet	$T_{an,in}$		740	°C
	FU_{stack}		75	%
	$\vec{x}_{an,in}$	CH_4	8	mol %
		CO	3	mol %
		CO_2	28	mol %
		H_2	21	mol %
		H_2O	40	mol %
Cathode inlet	$T_{cat,in}$		670	°C
	OU_{stack}		≤ 40	%
	$\vec{x}_{cat,in}$	O_2	21	mol %
		N_2	79	mol %

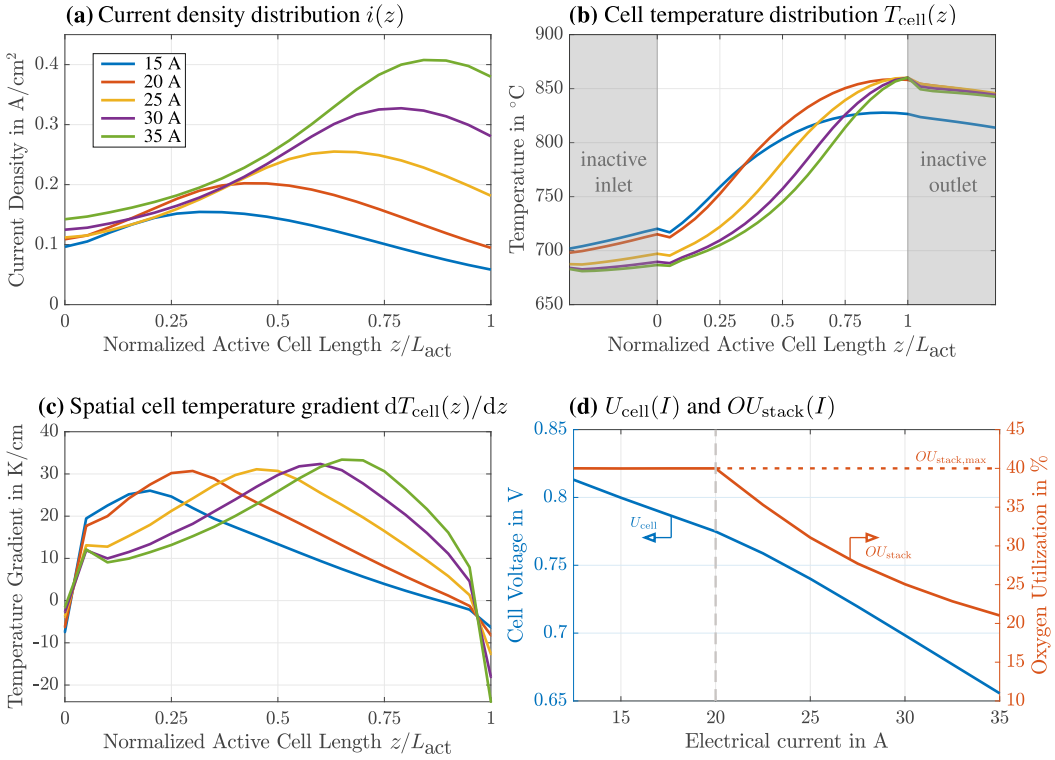

Figure 7. The spatial distribution of the electrical current (**a**), cell temperature (**b**), and its spatial gradient (**c**) along the flow coordinate for a set of electrical currents and gas inlet conditions, as given in Table 3. Cell Voltage and oxygen utilization as a function of the electrical current given in (**d**).

It becomes apparent that both the location of the peak current density and the maximum spatial temperature gradient shift from the end to the front of the cell for decreasing electrical current. The peak thermal gradient only decreases slightly at values above 30 K cm^{-1} as long as the target temperature is reached. Following the approach of van Biert, only the peak spatial temperature gradient $|dT_{cell}/dz|_{max}$ is used as an overall evaluating quantity of the thermal stress along the cell surface for the following system investigation. From a system perspective, thermal gradients are not only influenced by the stack characteristics itself but mainly by the heat recuperation capability of the adjacent plate heat exchangers.

4.2. Steady-State System Behavior

The coupled operating behavior of FCM and FPM is now investigated with regard to the system's net efficiency, thermal gradients inside the stack, and possible operating windows. Figure 8b shows the cell voltage as a function of system net power for begin of life (BoL, $t_{op} = 0$ h) in blue for identical O/C at FU_{stack} and RR as for the stack simulation in the previous section. It can be observed that the voltage level is generally lower compared to Figure 7d and that the OU_{stack} limitation is already reached at a higher current of 25 A. Furthermore, the cell voltage decreases for lower currents which could not be observed at stack operation with constant inlet conditions. This effect is due to lower average cell temperatures caused by lower inlet temperatures of both air and anode gases due to the worse heat exchange effectiveness of the recuperator heat exchangers at reduced partial load mass flows. Operation within the discussed limits is possible for the range of 5 to 15 kW, which corresponds to a load range of 33 to 100 %. For comparison, the voltage characteristics for degraded stacks after 10 kh of operation is depicted in red which shows a much more reduced operating range from around 6 to 11 kW, thus 40 to 73 % of load range.

Figure 8a,c–h depicts the stationary operating maps for the electrical currents 15, 20, 25, and 30 A, respectively, at BoL on the left, and after the 10 kh operation on the right. The depicted squares in blue and red correspond to the cell voltages in Figure 8b at $FU_{stack} = 75$ % and $RR = 70$ %.

In addition to the limits of each valid operating map, the system's net efficiencies are shown as grey contour lines and the maximum spatial cell temperature gradients as color gradients. Regarding the operating limits, the largest operating windows occur at intermediate and low electric loads at BoL and decrease both for higher currents and increasing degradation. The O/C_{min} limitation defining the minimum recirculation ratio occurs in the range of $O/C = 2.38$ and 2.5 at high electrical currents, depending on the system fuel utilization and the associated heat input in the pre-reformer. At lower electrical currents, O/C_{min} slightly increases to values between $O/C = 2.4$ and 2.53 due to slightly lower adiabatic pre-reformer temperatures, visible as a small shift of the O/C_{min} line to the right. The lowest permissible recirculation ratio of 68 % occurs at $FU_{stack,max}$ and 30 A BoL.

Furthermore, operating at high electrical currents and lower stack fuel utilizations is only possible to a limited extent due to the anode pressure limitation and the chosen design component pressure drops. At partial load, lower mass flows and associated lower pressure drops also allow operating at significantly lower utilizations.

The cell voltage is generally lowest at high recirculation ratios and high fuel utilizations due to lower values of the Nernst voltage. At BoL, cell voltage limitation is visible only in partial load in Figure 8g caused by high ASR values due to low cell temperatures. This phenomenon occurs more intensely with degraded stacks at already lower recirculation ratios in Figure 8h and additionally at the highest electrical load in Figure 8d due to the combination of high electrical current and high ASR values.

Independent from stack degradation and load conditions, the highest permissible system net efficiency is generally achieved in the corner area of $FU_{stack,max}$ and O/C_{min}, confirming the evaluation of similar system models with AOGR reported in the literature [12,13], with the overall highest efficiency of 59.8 % achieved at 25 A BoL, $FU_{stack,max}$, and $RR = 68.5$ %. As can be seen by the color gradients, however, the thermal stress of the stack reaches its maximum in this operating range as well, leading to up to 34.8 K cm^{-1} under the aforementioned conditions. At lower electrical currents, the thermal gradients decrease noticeably as the $OU_{stack,max}$ limitation leads to lower stack outlet temperatures, comparable to Figure 7c. Thermal gradients well below 30 K cm^{-1} at high electrical currents can be achieved by increasing the recirculation ratio significantly to values above 80 %, however at the cost of efficiency decrease of roughly 2 %-points.

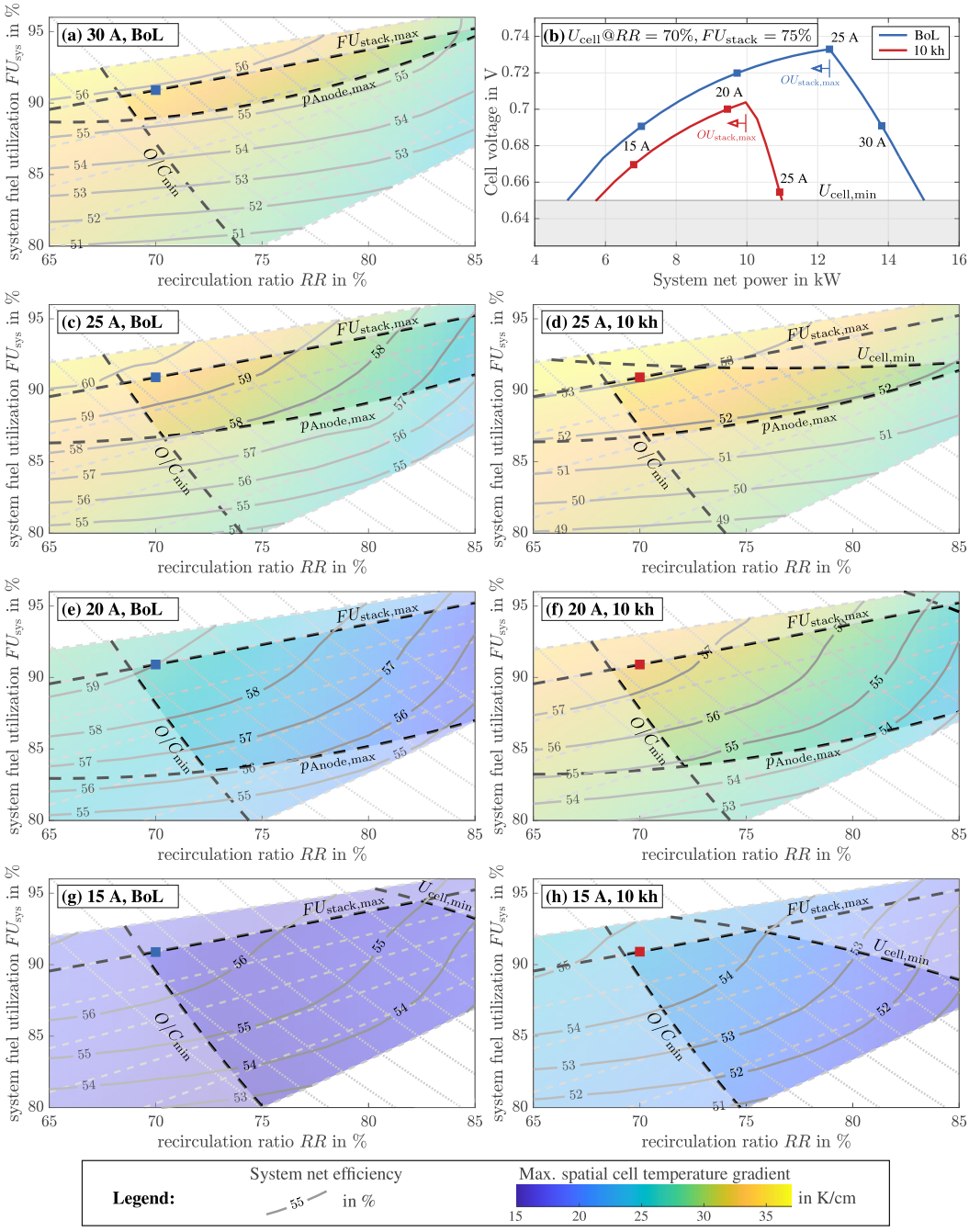

Figure 8. Steady-state operating maps of the SOFC system for a set of four electric currents for 'Begin of Life' (BoL) (left) and 10,000 h of operation (right). Cell voltage as a function of the electrical system net power (**b**).

To summarize, the steady-state operation of the investigated SOFC AOGR system is highly constrained by the presented set of system parameters that lead to non-uniform operating maps for different load and aging conditions of the stack. This already results in the need for precise and robust control in order to avoid operation outside the limits and associated degradation effects as far as possible. With regard to the transient system analysis in the next section, the operating point defined by $RR = 70\,\%$ and $FU_{stack} = 75\,\%$ marked with the blue and red squares is chosen both due to its generally high system net efficiency and its overall validity under all investigated system operating conditions.

5. Transient Simulation Results

Additional constraint violations and operating limitations occur during the envisaged dynamic system operation. The following studies are intended to provide guidance for the design and parameterization of a model predictive controller, as the system shall be permanently operated close to $FU_{\mathrm{stack,max}}$ and O/C_{min} and must be guided safely along these operating limitations during load changes. As stated above, this publication is limited to the investigation of the plant behavior itself and does not consider the closed-loop behavior and the respective controller. A typical approach would include an open-loop response analysis utilizing MV step changes, resulting in an extensive set of responses due to the mutual interaction of six MVs. Instead, a more application-relevant approach is chosen in this study by analyzing linear upward and downward ramps of all six MVs between their respective steady-state values listed in Table 4. The focus is mainly drawn on the anode loop and the interaction of the three directly involved MVs considering the impact of gas delay and thermal component inertia. Transient simulation is performed in Matlab Simulink with a stiff *ode15s* DAE solver using a fixed time step of 0.1 s.

In the following, the load reduction (ramp-down (↘ RD)) and load increase (ramp-up (↗ RU)) dynamics are discussed separately. Furthermore, the upward ramps are investigated starting from two distinctly different thermal states to account for the thermal system dynamics: a so-called hot ramp-up (HRU) is executed in close succession to a ramp-down with component temperatures still high due to the thermal inertia. In contrast, the cold ramp-up (CRU) refers to a start from a complete steady state with lower partial load component temperatures, as listed in Table 4, corresponding to a previous partial load operation of multiple hours.

Table 4. Stationary system parameters for selected full and partial load operating points used for the dynamic system simulation.

Parameter	Full Load BoL	Partial Load BoL	Unit
Manipulated Variables			
I	30	15	A
$f_{\mathrm{bl,rec}}$	176.55	118.21	Hz
$\dot{n}_{\mathrm{fuel}}$	0.0308	0.0154	$\mathrm{mol\,s^{-1}}$
$\dot{n}_{\mathrm{air,cat}}$	0.962	0.333	$\mathrm{mol\,s^{-1}}$
$\dot{n}_{\mathrm{air,OXU}}$	0.090	0.026	$\mathrm{mol\,s^{-1}}$
System Parameters			
FU_{stack}	75	75	%
RR	70	70	%
U_{cell}	0.691	0.688	V
$P_{\mathrm{sys,net}}$	13.81	6.99	kW
$T_{\mathrm{cell,av}}$	761.6	674.1	°C
$T_{\mathrm{cell,max}}$	860.0	738.25	°C
OU_{stack}	27.7	40	%
T_{adRef}	454.6	423.3	°C
O/C_{min}	2.479	2.523	-
Accumulated gas delay times			
$\Delta t_{\mathrm{bl,rec}\rightarrow\mathrm{stack}}$	5.6	12.2	s
$\Delta t_{\mathrm{stack}\rightarrow\mathrm{bl,rec}}$	3.5	7.5	s

5.1. Ramp-Down

First, a load reduction from 30 to 15 A with a ramp rate of 15 A $\mathrm{min^{-1}}$ is considered, thus resulting in a ramping interval of 60 s. Four ramp-down scenarios, labeled ↘ RD1 to ↘ RD4 in Table 5 and Figure 9 are considered, which differ with respect to the actuation of the MVs relevant to the anode loop ($\dot{n}_{\mathrm{fuel}}$, I, $f_{\mathrm{bl,rec}}$). The three remaining MVs, namely the cathode and oxidation unit airflow as well as the coolant flow, would need to be controlled

in order to avoid a temperature overshoot of the stack, oxidation unit, and recirculation blower, respectively. As they only affect the anode loop with a delay due to thermal inertia, the impact of these MVs is not part of this study; thus, these parameters are ramped identically for all scenarios considered.

Table 5. List of ramp start times for the four ramp-down scenarios at a constant ramp duration of 60 s, depicted in Figure 9.

	$\dot{n}_{\text{fuel}}$	I	$f_{\text{bl,rec}}$	Gas Delays Δt
↘ RD1	t_0	t_0	t_0	$\Delta t_i = 0$
↘ RD2	t_0	t_0	t_0	enabled
↘ RD3	t_0	$t_0 + \Delta t_{\text{bl,rec}\to\text{stack,30A}}$	$t_0 + \Delta t_{\text{bl,rec}\to\text{stack,30A}} + \Delta t_{\text{stack}\to\text{bl,rec,30A}}$	enabled
↘ RD4	t_0	$t_0 + \Delta t_{\text{bl,rec}\to\text{stack,30A}}$	$RR = 70\,\% = \text{const.}$	enabled
↗ HRU1	t_0	t_0	t_0	$\Delta t_i = 0$
↗ HRU2	t_0	t_0	t_0	enabled
↗ HRU3	t_0	$t_0 + \Delta t_{\text{bl,rec}\to\text{stack,15A}}$	$t_0 + \Delta t_{\text{bl,rec}\to\text{stack,15A}} + \Delta t_{\text{stack}\to\text{bl,rec,15A}}$	enabled
↗ HRU4	t_0	$t_0 + \Delta t_{\text{bl,rec}\to\text{stack,15A}}$	$RR = 70\,\% = \text{const.}$	enabled
↗ HRU5	t_0	$t_0 + \Delta t_{\text{bl,rec}\to\text{stack,15A}}$	$RR: 70\,\% \nearrow 80\,\% \searrow 70\,\%$	enabled
↗ CRU5	t_0	$t_0 + \Delta t_{\text{bl,rec}\to\text{stack,15A}}$	$RR: 70\,\% \nearrow 80\,\% \searrow 70\,\%$	enabled
↗ CRU6	t_0	$t_0 + \Delta t_{\text{bl,rec}\to\text{stack,15A}}$	$RR: 77.5\,\% \nearrow 80\,\% \searrow 70\,\%$	enabled

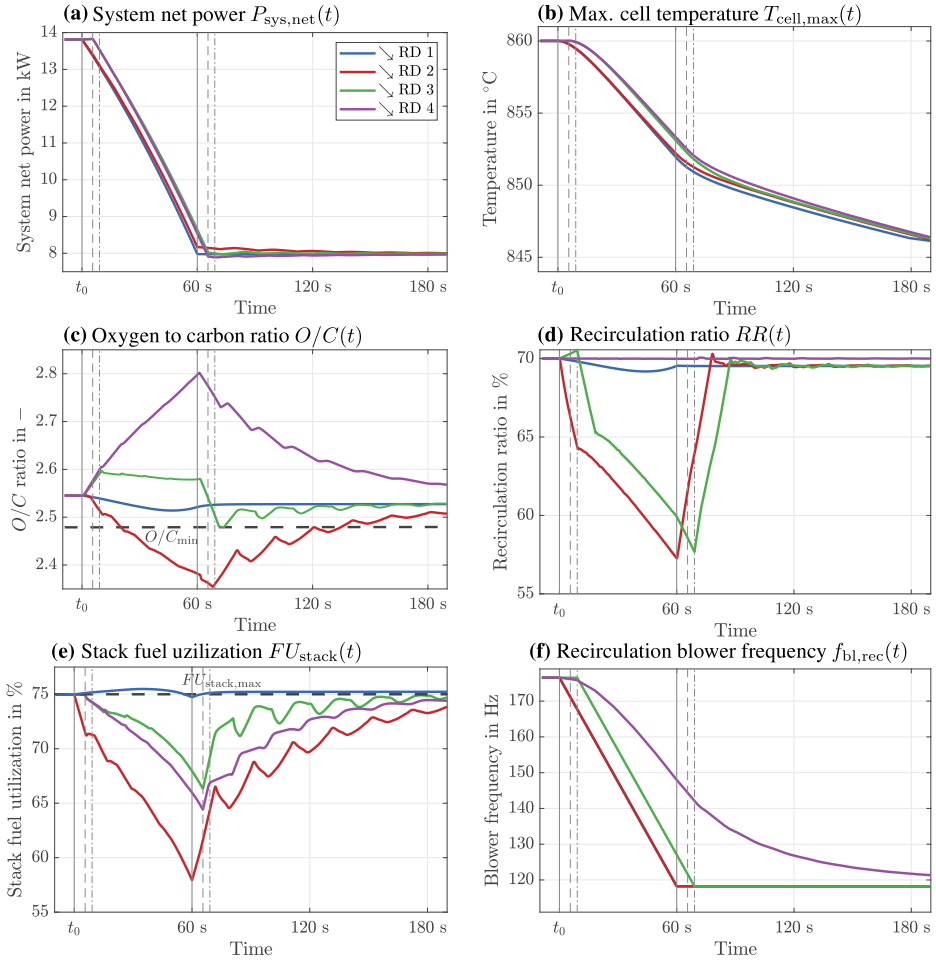

Figure 9. Transient load reduction simulations by means of four MV ramp-down strategies ↘ RD1 − 4 at an identical current ramp rate of 15 A min^{-1}. Ramp specifications are given in Table 5. The vertical lines depict the offset ramp start and end times of fuel flow (solid), electrical current (dashed) and blower frequency (dot-dashed).

The general dynamic system behavior is presented by first analyzing the idealized load change: the simultaneous reduction of all MVs from the steady-state full-load operating point at the identical time t_0. To illustrate the impact of the gas delay times (Equation (26)), a distinction is made between a load reduction neglecting (↘ RD1) and considering the gas delay times (↘ RD2). The corresponding characteristic system parameters during and shortly after ramping are shown in the plots of Figure 9 as blue and red lines, respectively.

In general, the similar immediate decrease of system net power at t_0 in Figure 9a and the associated temperature drop due to the decreasing dissipative heat in the stack in Figure 9b are visible for both ramp-down scenarios. Regarding the scenario without consideration of gas delays (↘ RD1), the characteristic anode loop parameters in Figure 9c–e almost remain unchanged, indicating that the amount of fuel supplied to the stack changes just according to the linearly decreasing electrochemical fuel demand. Furthermore, as the decreasing inlet fuel flow mixes with the immediately decreasing anode off-gas at the blower inlet, the molar composition and, thus, the O/C ratio in the pre-reformers remain almost constant. The slight deviation of the RR after the end of the ramp is due to the still high temperature levels compared to the partial load steady-state conditions for which the blower frequency was determined. This leads to slightly higher component pressure drops which in turn result in a slightly lower recirculated mass flow according to the blower characteristics.

A comparison of these results with the ↘ RD2 scenario, taking into account the gas delay times, shows a clear violation of O/C_{min}, while the fuel utilization drops significantly to values as low as 60 %. This effect is due to the delayed reduction of fuel flow at the anode inlet compared to the electrical current, caused by the accumulated gas delay time from the flow inlet to the stack $\Delta t_{\mathrm{bl,rec}\rightarrow\mathrm{stack,30A}}$, which causes a significant amount of excess fuel in the system. Additionally, as the delayed mass flows and, thus, the pressure drops are still high, the immediate reduction of blower frequency results in a drop of recirculated mass flow recognizable as a drop of RR during the ramping process. As a result of the reduced recirculation of H_2O, CO, and CO_2, the O/C ratio is reduced and remains below the limit both during the ramp time and the following minute.

The phenomena of interim excess fuel and reduced recirculation are now counteracted by lowering I and $f_{\mathrm{bl,rec}}$ with a time delay to the fuel supply (↘ RD3). The electrical current is thereby delayed by the cumulative gas delay time between the recirculation blower and stack entry at full load conditions, while the blower frequency is delayed by the total gas delay time of the anode loop to dilute the fuel. These offsets are indicated in the plots of Figure 9 as vertical dashed and dot-dashed lines.

The impact of the offset ramps can be seen in Figure 9c,f, as the O/C ratio remains above the threshold value and the fuel excess is reduced. In theory, this load change can be regarded as permissible. However, the O/C drop toward the end of the ramp poses an operation risk and is caused by the fact that the gas delay times increase significantly at lower electrical load and lower mass flows and reach more than twice as high values for part-load operation. This effect could be overcome by applying slightly diverging ramps to the MVs with the electrical current and blower frequency reaching its final value at even later time steps. In this study, another approach is chosen to highlight another suitable ramp-down scenario by adjusting the recirculation blower frequency in a way that the recirculation ratio remains at a constant value of 70 %, thus not applying a linear ramp (↘ RD4). The fuel and electrical current ramps remain unchanged from the previous scenario ↘ RD3. As can be seen in Figure 9f, the frequency is now lowered much later and remains at a higher value well after the ramping of fuel and electrical current have finished. This results in a distinct overshoot of O/C away from the minimum threshold during and shortly after the load change as a much higher amount of AOG is fed back to the pre-reformers.

Both ↘ RD3 and ↘ RD4 represent a theoretically suitable load reduction strategy for the arbitrarily chosen current ramp rate of 15 A min^{-1}, with ↘ RD3 being more critical in terms of O/C. These two strategies are further evaluated with regard to higher ramping speeds in Figure 10, where the solid and dashed blue lines are identical to ↘ RD3 and ↘ RD4 in Figure 9.

The most distinct difference between the two strategies at different speeds is the course of O/C in Figure 10c. The characteristic drops of ↘ RD3 at the end of ramping decrease further at higher ramp speeds and, thus, lead to violations of O/C_{min}. In contrast, the overshoots of ↘ RD4 further increase at higher speeds, thus enabling a load reduction for even higher current ramps. However, this will be limited in reality by an unacceptably high thermal stress of the stack, represented by the maximum time gradient of cell temperature for the three ramp rates in Figure 10d in K min^{-1}. For the investigated co-flow stack arrangement, the maximum temperature time gradient occurs at the end of the active cell area as the current density change during load reduction and, thus, the change in dissipative heat is the highest (compare Figure 7a). The maximum permissible current ramp-down rate is subject to the implemented cell geometries and material and has to be determined by an experimental investigation of tolerable temperature gradients without risk of cracking or delamination.

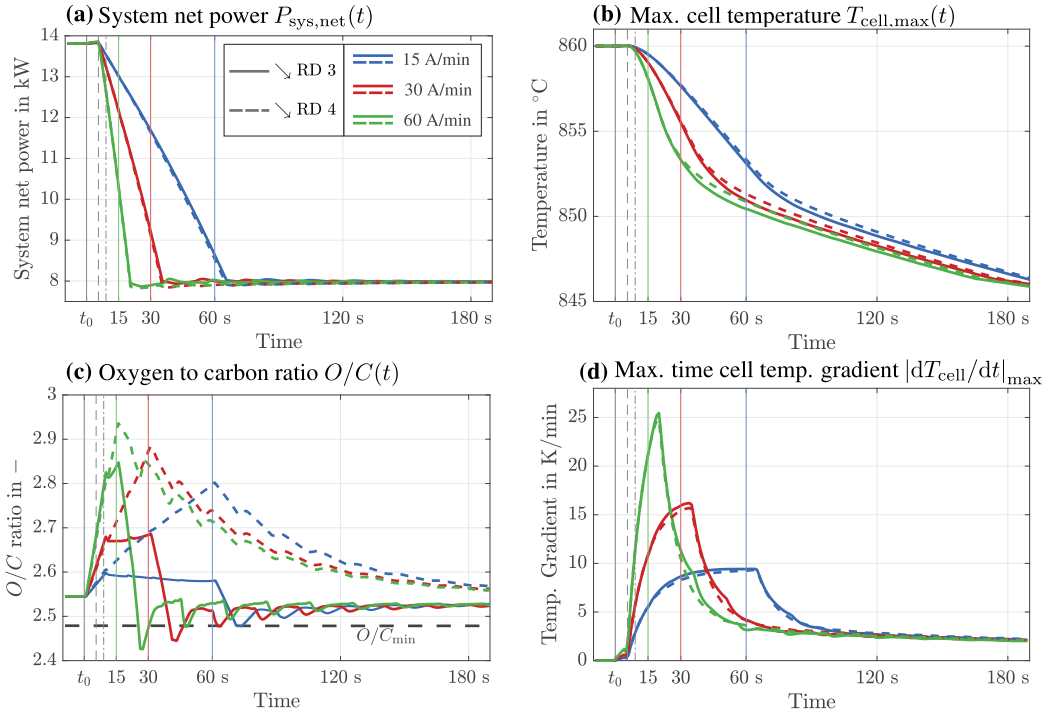

Figure 10. Transient load reduction simulations of selected ↘ RD3 and ↘ RD4 scenarios at three different current ramp rates of 15, 30, and 60 A min^{-1}. Ramp specifications are given in Table 5. The vertical black lines depict the offset ramp start times of fuel flow (solid), electrical current (dashed) and blower frequency (dot-dashed). The coloured solid vertical lines depict the corresponding fuel flow ramp end time.

5.2. Hot Ramp-Up

In analogy to the ramp-down investigation in the previous section, the simultaneous ramping of MVs neglecting (↗ HRU1) and considering gas delay times (↗ HRU2) are depicted in Figure 11 as reference cases in blue and red lines, respectively. The idealized ↗ HRU1 ramp-up again leads to a smooth course of O/C, FU_{stack}, and RR. Under consideration of the delays, the reverse system parameter effects compared to the observed ramp-down courses (↗ RD2) occur. On the one hand, the fuel reaches the stack only after a significant delay, resulting in a FU_{stack} overshoot above 90 %. On the other hand, the simultaneous increase in blower frequency causes the RR to rise sharply. The now higher mixing ratio of AOG to fuel leads to an increase in the O/C ratio.

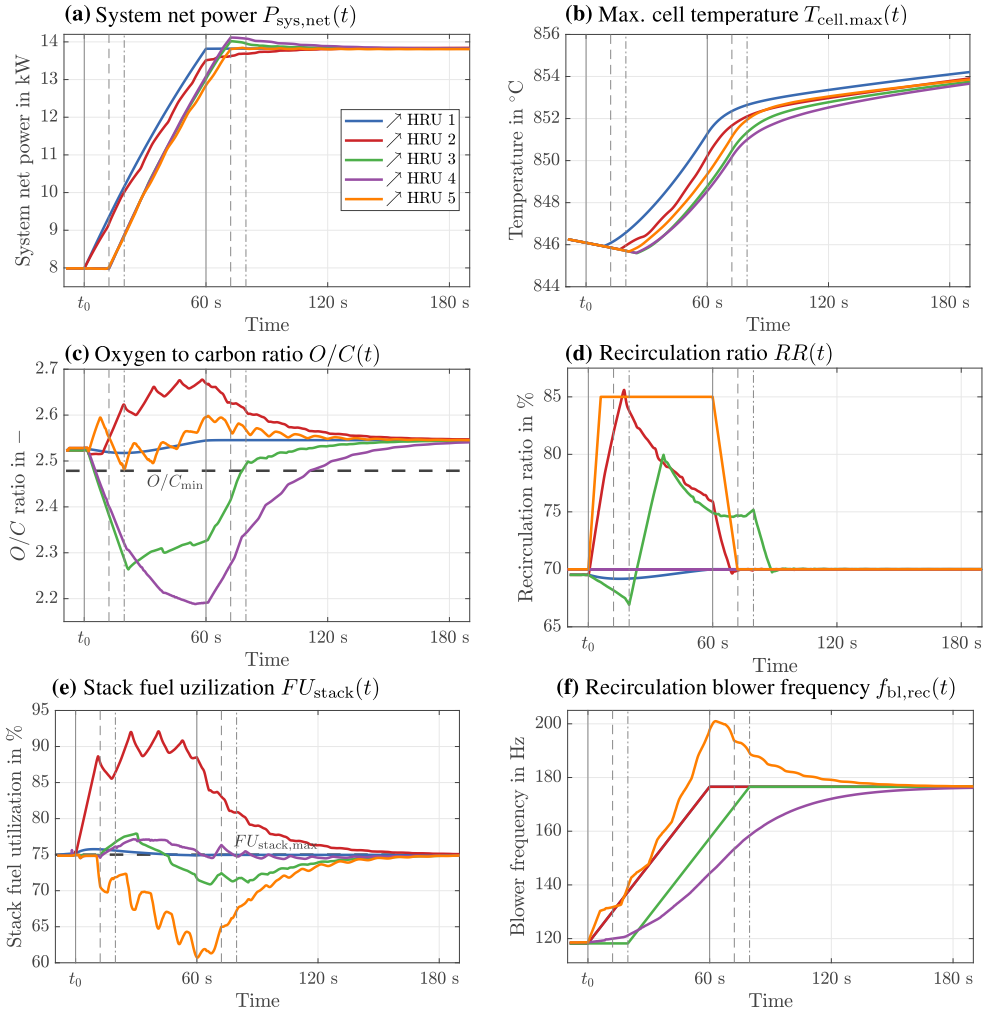

Figure 11. Transient load increase simulations started immediately after the load reduction of Figure 9 at high component temperatures (hot ramp-up) by means of five MV ramp-up strategies ↗ HRU1 – 5 at an identical current ramp rate of 15 A min^{-1}. Ramp specifications are given in Table 5. The vertical lines depict the offset ramp start and end times of fuel flow (solid), electrical current (dashed) and blower frequency (dot-dashed).

Analogous to the permissible ramp-down strategies ↘ RD3 and ↘ RD4, we illustrate the equivalent load increases with a delayed ramp-up of the current, along with an additional delay in ramping up the frequency (↗ HRU3), or an actuation of the blower frequency to maintain a constant RR of 70 % (↗ HRU4). Figure 11e indicates that the overshoot of FU_{stack} is now significantly lower for both cases. However, the later increase of the blower frequency leads to a drastic undershoot below O/C_{min} in both cases. Thus, a significantly different and earlier actuation of the blower is necessary. For this purpose, in a further scenario ↗ HRU5, the blower is actuated in such a way that the RR is ramped to a value of 85 % at the beginning of the fuel ramp t_0 and held there during the entire electrical current ramp duration (see Figure 11d). The corresponding blower frequency is initially somewhat steeper than the reference cases ↗ HRU1 and ↗ HRU2 and exhibits a maximum at the end of the ramp that is well above the steady-state full load value. The O/C ratio remains in the valid range and roughly follows the idealized curve of ↗ HRU1. This significant increase of the recirculated mass flow during the load increase represents the only permissible strategy from the scenarios presented here but requires knowledge of the transient system behavior in order to be able to drive the blower correctly.

5.3. Cold Ramp-Up

The load increase, starting from a steady-state partial load operating point, can be considered as the most demanding load change. Additional constraints due to low component temperatures arise, such as a slightly higher O/C_{min} value and significantly higher voltage losses in the stack, which in turn may lead to minimum cell voltage violations. Such a scenario is shown exemplarily in Figure 12 (↗ CRU5) by applying the same anode loop MV inputs as for the previously discussed suitable hot ramp-up strategy ↗ HRU5. However, the cathode airflow is now constantly held as low as possible ($OU_{\text{stack}} = OU_{\text{stack,max}}$) for the entire simulation time to ensure the fastest possible heating of the stack. In contrast to the hot ramp-up, this analysis depicts not only the immediate system behavior during the first three minutes but also the long-term thermal behavior over two hours. This is illustrated by means of a second time interval with a higher time scale after 200 s, as marked by the black vertical line.

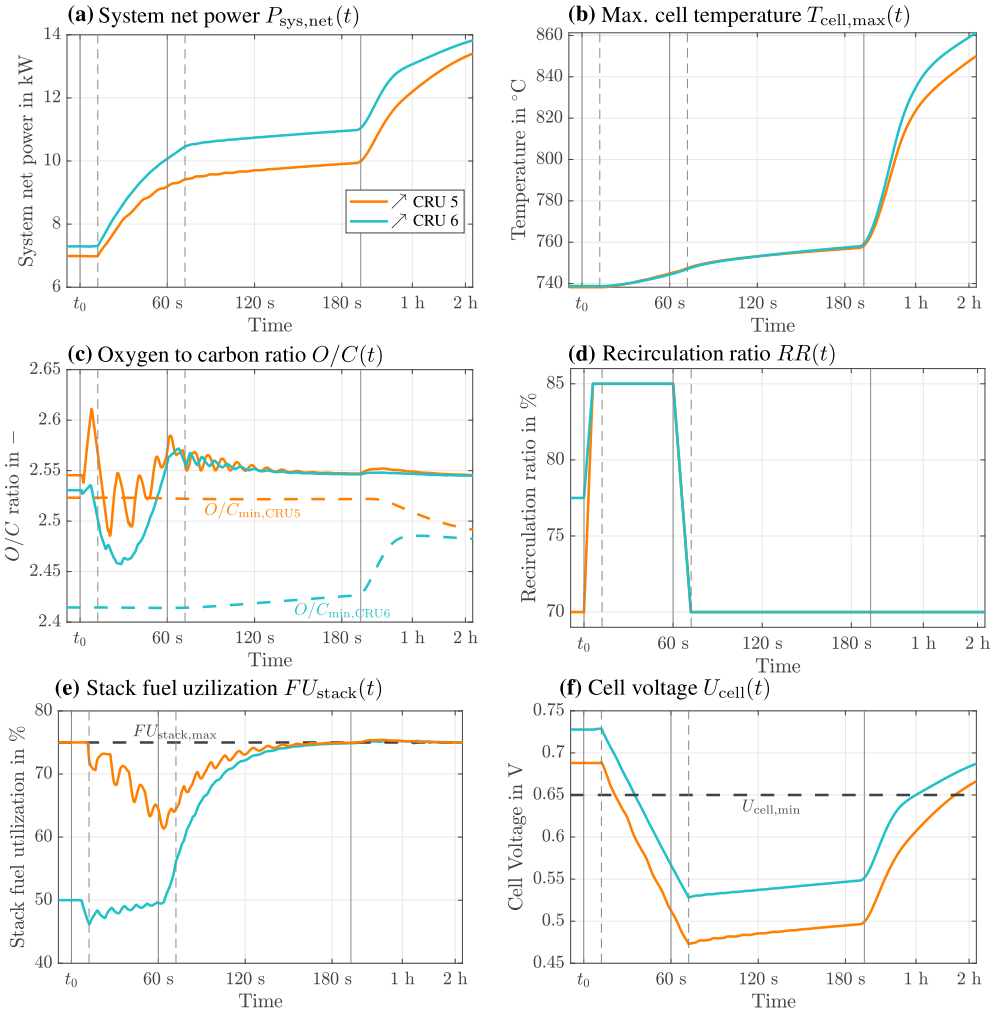

Figure 12. Transient load increase started from steady-state partial load operating points at lower component temperatures. Selected scenarios starting from $RR = 70\,\%$, $FU_{\text{stack}} = 75\,\%$ (↗ CRU5) and $RR = 77.5\,\%$, $FU_{\text{stack}} = 50\,\%$ (↗ CRU6). Ramp specifications are given in Table 5. The vertical lines depict the offset ramp start and end times of fuel flow (solid) and recirculation ratio (dashed).

While similar results to the hot ramp-up occur with regard to O/C, RR, and FU_{stack} depicting the gas flow dynamics and distribution, the course of cell voltage in Figure 12f and, consequently, the system net power in Figure 12a are heavily affected by the low stack temperature and lead to violations of the cell voltage minimum constraint. Due to the large thermal inertia of the stack, both the cell temperature and the cell voltage only increase

gradually over time and cell voltage recovers to tolerable values only after 100 minutes. The high thermal inertia of the stack could be overcome by additional components like electrical heaters or burners, which were part of a previous system study [7], but will not be considered here.

It becomes apparent that a model-based controller needs to be able to (i) limit the current ramp as soon as the voltage minimum is reached and (ii) adapt the fuel flow and the blower frequency accordingly. As this constrained load increase will lead to considerably longer load change times, a further measure (with no additional hardware) is presented, which is particularly of interest if the speed of the load change is of higher importance than the partial load and interim system efficiency (↗ CRU6). This is done by starting from a steady-state partial load operating point with a much lower fuel utilization to lift the overall cell voltage level. In accordance with the corresponding operating map (Figure 8g), a suitable partial load operating point at $FU_{\text{stack}} = 50\,\%$ and a higher $RR = 77.5\,\%$ is chosen. This corresponds with an efficiency decrease of 3.5 %-points. Linear ramping of the fuel flow and electrical current to reach the full load operating point at high fuel utilization is maintained. The previously presented strategy with high RR values during ramping is adopted to ensure suitable O/C values (see Figure 12c,d). The positive effect on the cell voltage can be seen in Figure 12f with an overall increase of roughly 45 mV, thus decreasing the time interval of minimum voltage violation. An interim lowering of fuel utilization could, thus, be considered a part of a constrained load increase strategy for a model-based system controller if temperatures are low.

6. Discussion

With regard to the modeling methodology explained in Section 3, validated modeling approaches from the literature were used in this study and, where possible, parameterized with experimentally obtained data on the component level. This is true for heat exchangers, the electrochemical cell behavior as well as the thermal inertia of the components. However, the remaining model characteristics need to be examined as well to confirm the validity of the chosen models. This concerns in particular the lumped CSTR approach for all BoP components simplifying the gas and solid interaction of each component to one energy balance and one temperature. If this is shown to be insufficient, model complexity needs to be increased accordingly at the cost of higher computation time. Extensive experimental testing on the system level has to be performed to ensure that all control-relevant physical interactions have been included in the proposed plant model. Secondly, the model deviation associated with the assumption of overall laminar pressure drops needs to be investigated and adjusted by means of obtained correlations, if necessary. Finally, the transient system behavior regarding the interaction of pressure drops, blower characteristics and the amount of recirculation needs to be validated by means of experimental MV step changes which will be performed prior to the implementation of MPC with the presented laboratory-scale system.

The previous section highlighted the challenges associated with the dynamic and efficient operation of a distributed SOFC AOGR system close to its operating constraints. It could be shown that a load decrease can be considered as the less demanding operation, as long as (i) the fuel supply is controlled considering the gas delay between fuel inlet and stack and (ii) the recirculation ratio is maintained at its target value by adjusting the blower frequency appropriately. In contrast, a load increase from an efficient operation at O/C_{min} and $FU_{\text{stack,max}}$ represents a more critical procedure, as the fuel flow is increased as the first actuation measure. This leads to critical gas mixtures with regard to carbon deposition, even when the recirculation ratio is kept constant. Thus, the recirculation blower frequency needs to be increased significantly in the moment of fuel increase to dilute the higher fuel flow with AOG. Additionally, low stack and component temperatures, occurring during an extended partial load operation, drastically limit the ability to increase the electrical load and the ability of the system to heat itself up.

In order to operate safely in the corner region of operating maps, a top-level system controller must be able to calculate the transient mass flow distribution in the anode loop

and actuate the MVs accordingly. This necessitates (i) the correct calculation of the actuation behavior of the recirculation blower, (ii) the correct calculation of the component pressure drops, and (iii) the correct calculation of gas delay times at any given full or partial load situation. This control task can be achieved by a model predictive controller that utilizes a suitable mathematical reduction of the presented system model as its internal prediction model. In addition, the MPC should comprise a prediction horizon of at least 60 to 120 s to fully account for the gas dynamics.

7. Conclusions

Within the scope of this publication, we investigated a methane-fueled SOFC system with anode off-gas recirculation (AOGR) regarding its applicability as an energy converter on board sea-going vessels. Compared to stationary applications, the use on vessels imposes significantly higher requirements for transient operating behavior in order to ensure load-following operation when combined with battery storage systems. The presented system plant layout consists of spatially separated fuel cell modules and a central fuel processing module to be used in an intermodal container.

For such a modular system, a first principle system model was developed, based on state-of-the-art model approaches from the literature, to serve as a starting point for model-based predictive system control (MPC). It consists of a spatially resolved model of a planar electrolyte-supported SOFC stack and lumped BoP component models utilizing a set of nonlinear differential-algebraic equations. Using this model, the steady-state and transient system behavior were analyzed. Special focus was placed on the limitation of the operating range by limiting variables, which are intended to prevent severe degradation of the stack or the pre-reformer catalyst. Five limitations were defined for this purpose in this study, namely a minimum cell voltage, a maximum stack oxygen, fuel utilization, a temperature-dependent minimum oxygen-to-carbon ratio (O/C), and a maximum anode overpressure.

Permissible steady-state operating maps for the entire electrical load range, as well as for two exemplary degradation states of the stack, were identified and evaluated with respect to system efficiency and thermal stress on the stack. For all presented steady-state load conditions, operating in the corner region of maximum stack fuel utilization and minimum O/C ratio was found to be the most efficient. However, these conditions are also associated with high thermal stress, especially at high current densities.

In a subsequent transient load change simulation study, the objective was to develop strategies for actuating the three relevant manipulated variables (MV) in the anode loop, namely the fuel flow, the electrical current, and the recirculation blower frequency, in order to enable permissible, fast, and efficient load changes. It was demonstrated that system interactions, caused by mass flow-dependent gas delays accumulating to up to 20 s in the anode loop of the investigated laboratory system under partial load conditions, significantly affect the control complexity near the operational constraints. Countermeasures were taken by choosing suitable MV actuation strategies to avoid overshoots of the stack fuel utilization or undershoots of O/C respectively. While the electrical current and fuel flow can be coordinated with the associated gas delay time between the fuel inlet and anode inlet to account for the remaining fuel in the corresponding gas volume, actuation of the recirculation blower frequency requires a deeper model understanding, as the recirculated mass flow and its composition are functions of the mass flow-dependent pressure drops in the anode loop and the blower characteristics. MV actuation strategies were demonstrated to successfully transition between the most efficient partial and full load steady-state operating points, close to maximum fuel utilization and minimum O/C, without constraint violation during or after the load change.

In a follow-up publication, the presented system model will be used to generate linearized state-space plant system models for a model predictive controller, which will be tested in a model-in-the-loop simulation environment. The observed system behavior and the developed MV actuation strategies will serve for MPC parameterization, specifically the prediction horizon, and the weights and constraints of the implemented cost function.

Author Contributions: Conceptualization, methodology, software, formal analysis, investigation, writing—original draft preparation, visualization, J.H.; writing—review and editing, supervision, project administration, and funding acquisition, S.K. All authors have read and agreed to the published version of the manuscript.

Funding: The authors gratefully acknowledge the financial support by the Federal Ministry of Transport and Digital Infrastructure, Germany (BMVI, funding code 03B10605H) and the coordination of the *MultiSchIBZ* project by the National Organisation Hydrogen and Fuel Cell Technology (NOW GmbH), Germany.

Data Availability Statement: Data are contained within the article.

Acknowledgments: The authors gratefully thank Marius Nozinski for his support in implementing the model in Matlab Simulink.

Conflicts of Interest: The authors declare no conflict of interest.

Abbreviations

The following abbreviations are used in this manuscript:

AOG	anode off-gas
AOGR	anode off-gas recirculation
ASR	area-specific resistance
DAE	differential-algebraic equation
DIR	direct internal reforming
ECR	electrochemical reaction
FCM	fuel cell module
FPM	fuel processing module
HEX	heat exchanger
HOR	hydrogen oxidation reaction
LHV	lower heating value
MPC	model predictive control
MSR	methane steam reforming
MultiSchIBZ	Multiple SchiffsIntegration Brennstoffzellen (German: Ship integration of multiple fuel cells (modules))
MV	manipulated Variable
ORR	oxygen reduction reaction
RD	ramp-down
RU	ramp-up
SOFC	solid oxide fuel cell
WGS	water–gas shift

Appendix A. Thermophysical Data Temperature Fits of Pure Gaseous Species

Table A1. Molar isobaric heat capacity and thermal conductivity temperature fits derived from NASA polynomials [33]. Temperature T in K.

	Molar Isobaric Heat Capacity $C_{m,p}(T) = a_c \cdot T^2 + b_c \cdot T + c_c$ in J mol^{-1}K^{-1}. Temperature Range: 300 K to 1173 K.			**Thermal Conductivity $\lambda(T) = a_\lambda \cdot T^2 + b_\lambda \cdot T + c_\lambda$ in W m^{-1}K^{-1}. Temperature Range: 473 K to 1173 K.**		
	a_c	b_c	c_c	a_λ	b_λ	c_λ
CH_4	-2.084×10^{-5}	8.478×10^{-2}	9.467	3.950×10^{-8}	1.426×10^{-4}	-1.455×10^{-2}
CO		6.441×10^{-3}	26.65	-1.745×10^{-8}	7.87×10^{-5}	3.384×10^{-3}
CO_2	-1.743×10^{-5}	4.568×10^{-2}	26.09		7.116×10^{-5}	-2.192×10^{-3}
H_2		2.2×10^{-3}	28.04		4.87×10^{-4}	3.634×10^{-2}
H_2O		1.228×10^{-2}	29.02		1.042×10^{-4}	-1.59×10^{-2}
O_2		7.058×10^{-3}	27.78		6.116×10^{-5}	1.128×10^{-2}
N_2		6.006×10^{-3}	26.61	-1.804×10^{-8}	7.513×10^{-5}	5.670×10^{-3}

Table A2. Dynamic viscosity-temperature fits derived from NASA polynomials [33] and molar masses. Temperature T in K.

	Dynamic Viscosity $\eta(T) = b_\eta \cdot T + c_\eta$ **in Pa s. Temperature Range: 473 K to 1173 K.**		**Molar Mass** M **in kg mol^{-1}.**
	b_η	c_η	
CH_4	2.262×10^{-8}	5.683×10^{-6}	16.043×10^{-3}
CO	3.352×10^{-8}	8.072×10^{-6}	28.01×10^{-3}
CO_2	3.298×10^{-8}	6.887×10^{-6}	44.01×10^{-3}
H_2	1.540×10^{-8}	5.037×10^{-6}	2.016×10^{-3}
H_2O	4.025×10^{-8}	-2.774×10^{-6}	18.015×10^{-3}
O_2	3.914×10^{-8}	1.124×10^{-5}	31.99×10^{-3}
N_2	3.408×10^{-8}	8.530×10^{-6}	28.013×10^{-3}

Table A3. Molar Gibbs reaction enthalpy temperature fits derived from NASA polynomials and reaction enthalpies at standard pressure and reference temperature T_0 for relevant chemical reactions [33]. Temperature T in K.

	Molar Gibbs Reaction Enthalpy $\Delta^R G^\Theta_m(T) = b_g \cdot T + c_g$ **in J mol^{-1}.**			**Molar Reaction Enthalpy** $\Delta^R H^\Theta_m(T_0 = 1000\ K)$ **in J mol^{-1}.**
	b_g	c_g	**Temp. Range**	
MSR (Equation (7))	-2.491×10^2	2.222×10^5	673 K to 1173 K	2.250×10^5
WGS (Equation (8))	3.266×10^1	-3.575×10^4	673 K to 1173 K	-3.476×10^4
ECR (Equation (6))	5.571×10^1	-2.483×10^5	973 K to 1173 K	-2.479×10^5
H_2 comb. (Equation (13))				
CO comb. (Equation (14))				-2.826×10^5
CH_4 comb. (Equation (15))				-8.012×10^5

Appendix B. Specific Isobaric Heat Capacities of Solid Materials

Table A4. Specific isobaric heat capacities of the considered component materials. Temperature T in K.

	Specific Isobaric Heat Capacity $c_p(T) = a_c \cdot T^2 + b_c \cdot T + c_c$ **in J kg^{-1}K^{-1}.**			
	a_c	b_c	c_c	**Temp. Range**
1.4828 [38]	-2.053×10^{-4}	4.841×10^{-1}	3.297×10^2	473 K to 1173 K.
Al_2O_3 [39]		2.888×10^{-1}	9.460×10^2	673 K to 933 K.

Appendix C. O/C_{min} Temperature Fit

The O/C_{min} temperature polynomial fit of the fifth order (shown in Figure 5 and deducted from threshold lines kindly provided by Jaworski et al. [37] at atmospheric pressure) is given as:

$$O/C_{min}(\vartheta) = -3.408 \times 10^{-14} \cdot \vartheta^5 + 1.382 \times 10^{-10} \cdot \vartheta^4 - 2.011 \times 10^{-7} \cdot \vartheta^3 + 1.315 \times 10^{-4} \cdot \vartheta^2 - 4.104 \times 10^{-2} \cdot \vartheta + 7.612, \quad \text{(A1)}$$

where ϑ is the temperature in °C. The valid O/C range for this fit is from 200 °C to 800 °C.

References

1. International Maritime Organization. *Fourth Greenhouse Gas Study 2020*; International Maritime Organization: London, UK, 2020.
2. DNV GL AS Maritime. Alternative Marine Fuels Study: Comparison of Alternative Marine Fuels. 2019. Available online: https://sea-lng.org/wp-content/uploads/2020/04/Alternative-Marine-Fuels-Study_final_report_25.09.19.pdf (accessed on 20 November 2023).
3. Kersing, A.; Stone, M. *The Shipping Industry's Fuel Choices on the Path to Net Zero*; McKinsey & Company: New York, NY, USA, 2023.
4. Weber, A. Fuel flexibility of solid oxide fuel cells. *Fuel Cells* **2021**, *110*, 651. [CrossRef]
5. Powell, M.; Meinhardt, K.; Sprenkle, V.; Chick, L.; McVay, G. Demonstration of a highly efficient solid oxide fuel cell power system using adiabatic steam reforming and anode gas recirculation. *J. Power Sources* **2012**, *205*, 377–384. [CrossRef]
6. Van Veldhuizen, B.N.; van Biert, L.; Amladi, A.; Woudstra, T.; Visser, K.; Aravind, P.V. The effects of fuel type and cathode off-gas recirculation on combined heat and power generation of marine SOFC systems. *Energy Convers. Manag.* **2023**, *276*, 116498. [CrossRef]
7. Hollmann, J.; Fuchs, M.; Spieker, C.; Gardemann, U.; Steffen, M.; Luo, X.; Kabelac, S. System Simulation and Analysis of an LNG-Fueled SOFC System Using Additively Manufactured High Temperature Heat Exchangers. *Energies* **2022**, *15*, 941. [CrossRef]
8. Valadez Huerta, G.; Álvarez Jordán, J.; Marquardt, T.; Dragon, M.; Leites, K.; Kabelac, S. Exergy analysis of the diesel pre-reforming SOFC-system with anode off-gas recycling in the SchIBZ project. Part II: System exergetic evaluation. *Int. J. Hydrogen Energy* **2018**, *44*, 10916–10924. [CrossRef]
9. Valadez Huerta, G.; Álvarez Jordán, J.; Dragon, M.; Leites, K.; Kabelac, S. Exergy analysis of the diesel pre-reforming solid oxide fuel cell system with anode off-gas recycling in the SchIBZ project. Part I: Modeling and validation. *Int. J. Hydrogen Energy* **2018**, *43*, 16684–16693. [CrossRef]
10. ShipFC project on first maritime fuel cell to run on green ammonia. *Fuel Cells Bull.* **2020**, *2020*, 5–6. [CrossRef]
11. Van Biert, L.; Visser, K.; Aravind, P.V. A comparison of steam reforming concepts in solid oxide fuel cell systems. *Appl. Energy* **2020**, *264*, 114748. [CrossRef]
12. Carré, M. *Modeling and Control of a Solid Oxide Fuel Cell System with Anode Offgas Recycle for Residential Combined Heat and Power Generation*; Der Andere: Leipzig, Germany, 2012; Volume 2012/1.
13. Peters, R.; Deja, R.; Blum, L.; Pennanen, J.; Kiviaho, J.; Hakala, T. Analysis of solid oxide fuel cell system concepts with anode recycling. *Int. J. Hydrogen Energy* **2013**, *38*, 6809–6820. [CrossRef]
14. Stiller, C. Design, Operation and Control Modelling of SOFC/GT Hybrid Systems. Ph.D. Thesis, NTNU, Trondheim, Norway, 2006.
15. Kistner, L.; Bensmann, A.; Hanke-Rauschenbach, R. Optimal Design of Power Gradient Limited Solid Oxide Fuel Cell Systems with Hybrid Storage Support for Ship Applications. *Energy Convers. Manag.* **2021**, *243*, 114396. [CrossRef]
16. Schäfer, F.; Egger, S.; Steiner, D.; Carré, M.; Eichel, R.A. Control of Oxygen-to-Carbon Ratio and Fuel Utilization with Regard to Solid Oxide Fuel Cell Systems with Anode Exhaust Gas Recirculation: A Review. *J. Power Sources* **2022**, *524*, 231077. [CrossRef]
17. Engelbracht, M.F.A. Design of a Highly Efficient Solid Oxide Fuel Cell System with Integrated Safety Gas Generation. Ph.D. Thesis, RWTH Aachen, Aachen, Germany, 2016.
18. Kupecki, J. Off-design analysis of a micro-CHP unit with solid oxide fuel cells fed by DME. *Int. J. Hydrogen Energy* **2015**, *40*, 12009–12022. [CrossRef]
19. Marra, D.; Pianese, C.; Polverino, P.; Sorrentino, M. *Models for Solid Oxide Fuel Cell Systems*; Springer: London, UK, 2016. [CrossRef]
20. Bessler, W.G.; Gewies, S.; Willich, C.; Schiller, G.; Friedrich, K.A. Spatial Distribution of Electrochemical Performance in a Segmented SOFC: A Combined Modeling and Experimental Study. *Fuel Cells* **2010**, *10*, 411–418. [CrossRef]
21. Braun, R.J. Optimal Design and Operation of Solid Oxide Fuel Cell Systems for Small-Scale Stationary Applications. Ph.D. Thesis, University of Wisconsin, Madison, WI, USA, 2002.
22. Aguiar, P.; Adjiman, C.S.; Brandon, N.P. Anode-supported intermediate temperature direct internal reforming solid oxide fuel cell. I: Model-based steady-state performance. *J. Power Sources* **2004**, *138*, 120–136. [CrossRef]
23. Engelbracht, M.F.A.; Peters, R.; Blum, L.; Stolten, D. Analysis of a Solid Oxide Fuel Cell System with Low Temperature Anode Off-Gas Recirculation. *J. Electrochem. Soc.* **2015**, *162*, F982. [CrossRef]
24. Van Biert, L.; Godjevac, M.; Visser, K.; Aravind, P.V. Dynamic modelling of a direct internal reforming solid oxide fuel cell stack based on single cell experiments. *Appl. Energy* **2019**, *250*, 976–990. [CrossRef]
25. Fang, Q.; Blum, L.; Peters, R.; Peksen, M.; Batfalsky, P.; Stolten, D. SOFC stack performance under high fuel utilization. *Int. J. Hydrogen Energy* **2015**, *40*, 1128–1136. [CrossRef]
26. Achenbach, E.; Riensche, E. Methane/steam reforming kinetics for solid oxide fuel cells. *J. Power Sources* **1994**, *52*, 283–288. [CrossRef]
27. Van Biert, L.; Visser, K.; Aravind, P.V. Intrinsic methane steam reforming kinetics on nickel-ceria solid oxide fuel cell anodes. *J. Power Sources* **2019**, *443*, 227261. [CrossRef]
28. Hering, M. Evaluation of the Effects of Varying Fuel Quality on Solid Oxide Fuel Cell Systems. Ph.D. Thesis, TU Clausthal, Clausthal, Germany, 2018. [CrossRef]
29. Qi, Y.; Huang, B.; Luo, J. Dynamic modeling of a finite volume of solid oxide fuel cell: The effect of transport dynamics. *Chem. Eng. Sci.* **2006**, *61*, 6057–6076. [CrossRef]
30. Çengel, Y.A.; Ghajar, A.J. *Heat and Mass Transfer: Fundamentals and Applications*, 6th ed.; McGraw-Hill Education: New York, NY, USA, 2020.

31. Walter, C.; Schwarze, K.; Boltze, M.; Herbrig, K.; Surrey, A. Status of Stack & System Development at Sunfire. In Proceedings of the 14th European SOFC & SOE Forum (EFCF); Luzern, Switzerland, 20–23 October 2020; pp. 29–38.
32. Marquardt, T.; Hollmann, J.; Gimpel, T.; Schade, W.; Kabelac, S. Femtosecond Laser-Induced Surface Modification of the Electrolyte in Solid Oxide Electrolysis Cells. *Energies* **2020**, *13*, 6562. [CrossRef]
33. McBride, B.J.; Gordon, S.; Reno, M.A. Coefficients for Calculating Thermodynamic and Transport Properties of Individual Species: NASA Technical Memorandum 4513; NASA: Washington, DC, USA, 1993.
34. Wilke, C.R. A Viscosity Equation for Gas Mixtures. *J. Chem. Phys.* **1950**, *18*, 517–519. [CrossRef]
35. Mason, E.A.; Saxena, S.C. Approximate Formula for the Thermal Conductivity of Gas Mixtures. *Phys. Fluids* **1958**, *1*, 361. [CrossRef]
36. Neidhardt, J. Nickel Oxidation in Solid Oxide Cells: Modeling and Simulation of Multi-Phase Electrochemistry and Multi-Scale Transport. Ph.D. Thesis, Universität Stuttgart, Stuttgart, Germany, 2013.
37. Jaworski, Z.; Zakrzewska, B.; Pianko-Oprych, P. On thermodynamic equilibrium of carbon deposition from gaseous C-H-O mixtures: Updating for nanotubes. *Rev. Chem. Eng.* **2017**, *33*, 42. [CrossRef]
38. Richter, F. The Physical Properties of Steel: Part I: Tables and Figures. 2011. Available online: https://www.tugraz.at/fileadmin/user_upload/Institute/IEP/Thermophysics_Group/Files/Staehle-Richter.pdf (accessed on 20 November 2023).
39. Ginnings, D.C.; Corruccini, R.J. Enthalpy, specific heat, and entropy of aluminum oxide from 0 degrees to 900 degrees C. *J. Res. Natl. Bur. Stand.* **1947**, *38*, 593–600. [CrossRef]